International Forum on Aeroelasticity and Structural Dynamics
IFASD 2024
17-21 June 2024, The Hague, The Netherlands

CONSTRAINED FLEXIBLE WING WITH FOLDING WINGTIP DYNAMICS MODEL BASED ON LAGRANGE'S METHOD

Lina Dehmlow[1], Pedro J. González[1], Gerrit Stavorinus[1], Flávio J. Silvestre[1]

[1]Technical University of Berlin
Marchstraße 12, 10587 Berlin, Germany
l.dehmlow@tu-berlin.de
p.gonzalez.ramirez@tu-berlin.de
g.stavorinus@tu-berlin.de
flavio.silvestre@tu-berlin.de

Keywords: Instructions, IFASD, structural dynamics, aeroelasticity

Abstract: One way of reducing an aircraft's induced drag while meeting airport gate limitations is increasing the wingspan and introducing a folding wingtip. By making the hinge flexible and rotating it's axis outboard the folding wingtip could be used to reduce gust loads. As aircraft are becoming more flexible, the flexibility is another important factor that needs to be considered. In the following a set of equations of motion describing a constrained flexible wing with a flared folding wingtip, that considers follower forces of the wing and folding wingtip as well as the geometric exact angle of attack is derived using Lagrange's method considering the folding wingtip as separate body. The formulation is used to set up an aeroelastic model in MATLAB/Simulink. The model is tested on the TU-Flex wing with a hinge introduced at $80\,\%$ span and compared to the original wing. It can be shown that the folding wingtip dynamics have an influence on the stability of the system reducing the damping of the modes and introducing a new lower frequency mode.

1 INTRODUCTION

One way of reducing an aircraft's induced drag and thereby improving the aircraft's efficiency is increasing the wing's aspect ratio and thereby the wing span. In order to meet airport gate limitations, the wingtips can be made foldable. The need to make the wingtips foldable, thereby adding extra weight, raises the question whether there are other advantages by using folding wingtips (FWT). Various studies suggest that hinge lines not parallel to the aircraft's symmetry plane could be used to reduce gust loads which would lead to reduced structural weight and thereby lighter aircraft and increased efficiency [1–13]. Another factor, that needs to be considered is that new materials like fibre composite materials together with increased aspect ratio lead to more flexible aircraft. Therefore, considering the aircraft flexibility to make sure no dangerous coupling exist and achieving considerable load alleviation are an important factor when using FWT [14–17].
The principle of load alleviation with FWTs is based on hinge lines rotated outboard (positive hinge angle Λ), as shown in figure 1 on page 5. In that case a negative folding angle θ (wingtip folded upwards) leads to a smaller incidence at the FWT and therefore a smaller angle of attack and a smaller lift in comparison to the case of zero fold angle position. Folding the wingtip downwards on the other hand increases the incidence at the FWT. For the case that the wingtip is brought out of its trim position (e.g. by a gust), this effect leads to the wingtip recovering its

original position.
The history of using FWTs to prevent aerodynamic overloads goes back to 1938 when Rouanet and Rey [1] first patented their invention for foldable wings with hinge lines not parallel to the aircraft symmetry plane and therefore not parallel to the flow.
In the meantime not much relevant research on that topic was published until in 2004 Pitt [2] analysed the effects of different hinge line angles in the context of aeroelastic tailoring using Nastran. They could show how FWTs can be used for static load alleviation, as described above, but also decrease flutter speeds compared to a baseline wing.
The flow and control characteristics of active controlled wingtips with hinges parallel to the flow were experimentally investigated by Gatto et al. [18]. They could show that FWTs can be used for roll control as well as to alleviate wing loads.
Pattinson et al. [3] coupled a flexible multi-body solver within a computational fluid dynamics structural model to analyse the load alleviation capabilities of FWTs. They also included local aerodynamic effects, such as local stall and transonic effects. The equations of motion were derived using the Lagrange method and a solver in Python using an implicit method. They could show the FWTs potential of alleviating wing loads.
The influence of nonlinear hinge springs, that only allow a wingtip deflection for larger loads was investigated by Castrichini et al. [4–6] in different papers. They used an aeroelastic aircraft model to analyse the gust load alleviation capabilities, the trim condition and aeroelastic stability. To calculate the angle of attack at the FWT α_{fw} they introduced the following small angle approximation:

$$\alpha_{\text{fw}} = -\arctan\left(\tan(\theta)\sin(\Lambda)\right). \tag{1}$$

In the model, wingtip deflections were modelled as local deformations so that wingtip shortening effects due to wingtip rotation were not considered. Also, follower forces for the FWT were not considered. They could show that the dynamic loads can be best reduced with a low hinge moment threshold, low damping values, low wingtip masses and a small hinge spring stiffness. For the trim condition they showed that the lift contribution of the FWT to the total lift is smaller for a smaller hinge spring stiffness, due to a larger fold angle. For low wingtip masses and a low hinge stiffness, they could show that the wingtip and airframe modes were uncoupled.
Cheung et al. [7] analysed the gust load alleviation capabilities of FWTs experimentally in low-speed wind tunnel tests and compared the results to a numerical model. The numerical Nastran model did only provide good results for fold angles close to zero and it is assumed that it was not able to describe the dependence between angle of attack and fold angle well.
Later Cheung et al. [8] proposed a new equation for calculating the angle of attack at the FWT as a function of angle of attack, hinge line and fold angle. In wind tunnel tests they confirmed earlier results showing that the peak wing root bending moment (WRBM) can be reduced using a FWT. They also introduced a wingtip tap at the FWT to provide active control of the FWT, which was shown to further reduce the peak WRBM.
Dussart et al. [14] used a reduced-order flight mechanics model of a flexible airplane with a foldable wingtip for a real-time simulation. They coupled a linear structural model with unsteady aerodynamics and ordinary flight dynamics equations of motion. To describe the twist angle change ε_{fw} at the FWT another small angle approximation was used:

$$\Delta\varepsilon_{\text{fw}} = -\arctan\left(\tan(\Lambda)\sin(\theta)\right). \tag{2}$$

They could show that flexible wings reduce the effect of FWTs compared to rigid wings.
AlbatrossONE is a Semi Aeroelastic Hinge (SAH) small scale demonstrator aircraft in which a free hinge was combined with a lock to release the hinge in case of large gust or manoeuvre

loads and then recover the wingtip to its original position. The demonstrator is a basic proof of concept demonstrator and therefore geometrically but not dynamically scaled. Various tests, including flight tests, showed that a reduction in bending loads and roll damping can be achieved for free wingtips. [9, 10]

The influence of FWTs with SAH on the flight dynamics was investigated by Castrichini et al. [11]. They used a practical mean axis reference frame to derive a linear set of equations of motion using the centre of gravity position, the Euler angles and the elastic model displacements as generalised coordinates. As in previous papers the wingtip rotation is described using a set of flexible modes. The hinge devices are then modelled by applying external moments. Unsteady aerodynamic effects are modelled using the doublet lattice method. They could show that the handling qualities and the dynamic response are similar to those of a reference aircraft without FWTs and that FWTs can be used for load reduction and to reduce roll damping.

Ajaj [19] analysed the influence of flared FWTs actively locked at different fold angles on wing root loads and flight dynamics. Common flight dynamics equations of motion are used and the geometric incidence at the FWT is calculated using equation 2. They showed that the folding wing is more effective in a rigid aircraft. Folding wingtips have little effect on the longitudinal flight mechanics but have an impact on the lateral flight mechanics, reducing the time constant of the spiral mode.

Conti et al. [20] used a multi-body formulation to describe the motion of a rigid FWT attached to a flexible aircraft that is fully constrained at the CG. That way follower forces at the FWT are considered. As they focussed on the static response of the FWT, they assumed a null inertia tensor for the FWT. They showed the importance of considering geometric nonlinearities, especially for high angles of attack.

Healy et al. [21] derived a geometric exact description of the angle of attack at the FWT as a function of aircraft angle of attack, sideslip angle, dihedral angle, hinge line angle, fold angle and geometric sweep. They derived the equation by transforming the airspeed into a FWT coordinate system, with the y-axis pointing along the leading edge of the FWT. The authors then developed an algorithm in MATLAB using MSC Nastran for static and dynamic aeroelastic analysis to use the geometric exact description. Additionally, it was shown that including geometric nonlinearities changes the flutter speed up to $28\,\%$. There was a good agreement between experimental and numerical data.

Sanghi et al. [15–17] showed the importance of considering wing flexibility in different papers. They used the coupled nonlinear aeroelastic-flight dynamics framework from the University of Michigan to investigate load alleviation capabilities, ride quality and roll control for different control surfaces including FWTs. For FWTs and flexible aircraft they could show that the load alleviation depends on the dynamic pressure. For higher dynamic pressure the released FWT leads to an increase of the local angle of attack of the inner wing, which can lead to higher loads. Deploying FWTs increased acceleration and therefore worsened ride quality. For low aerodynamic pressure the free FWTs did not have an impact on roll manoeuvres commanded by a trailing edge control surface but for higher dynamic pressured the aircraft rolled slower.

Balatti et al. [22] derived simplified equations of motion using the displacement in z-direction, the angle of attack, the wing bending and torsion and the wingtip folding angle as degrees of freedom and used a multi-objective optimization to minimize the gust response in the flight envelope.

Later Balatti et al. [12, 13] used the results of structural and wind tunnel gust response tests to validate an aeroelastic model and then use the model for time domain simulation of an active wingtip. Due to the geometric nonlinearities the numerical model only predicted the initial part of the fold angle history and the maximum peak of the WRBM correctly. The numerical results

of the active wingtip showed a Proportional-derivative (PD) controller's ability to alleviate the maximum vertical hinge displacement and the WRBM.
The effects of FWTs on the flight mechanics and handling qualities were experimentally investigated by Gu et al. [23]. For a straight wing they could show that the FWT has little influence on the longitudinal static stability. For a swept wing the longitudinal stability decreased. They could show that the wingtip fold angle reached 90° when the sideslip angle was equal to the hinge flare angle.
In none of the above studies a flexible free-flying aircraft with FWT, modelled with nonlinear dynamics using multi-body dynamics and the geometric exact angle of attack at the FWT was studied so far. The consideration of these effects may have a major impact on the overall stability (aeroelastic and flight mechanical) of the vehicle, especially when the wing's structural flexibility increases. Different authors could show that the flexibility has a large influence when it comes to load alleviation as well as flight mechanics and handling qualities of aircraft with FWTs [14–17, 19]. As modern aircraft are build with fibre composite materials which result in more flexible aircraft, the aircraft's flexibility is an important factor to consider when analysing the capabilities of FWTs. Also, a multi-body formulation is needed to better assess the influence between aircraft and FWT and to make sure no coupling between the structural and FWT modes exist within the flight envelope. Another important aspect is the description of the forces at the FWT which involves using a geometric exact formulation for the angle of attack at the FWT [20, 21].
The objective of the present work is to derive a set of equations of motion with Lagrange's method as in Waszak and Schmidt [24], to describe the dynamics of a constrained flexible wing with flared FWT, considering the FWT as separate body. The elastic displacements are described using modal shapes assuming linear structural dynamics. To describe the geometric angle of attack at the FWT the approach described by Healy et al. [21] is adapted to the used formulation and extended for also considering the incidence change due to flexibility. For the aerodynamics, unsteady effects due to elastic displacements of the inner wing will be considered as in [25]. Also, follower forces on the wing and FWT will be considered. The derived set of nonlinear dynamics equations will be tested on the constrained TU-Flex wing with FWTs and compared to a similar wing without FWTs. The aeroelastic stability of both wings will be compared for different hinge stiffness and hinge damping coefficients. The findings will be used to develop a fully coupled aeroelastic flight dynamical model considering the aircraft flexibility as well as the multi-body dynamics of the FWT in the future.

2 THEORETICAL BACKGROUND

In the following the equations of motion for a clamped wing possessing a FWT will be derived using Lagrange's equation. Firstly, the reference frames and kinematics of the wing are defined. Then kinetic and potential energy expressions are derived, which are then inserted into Lagrange's equation. In a next step the generalised loads are derived and the formulation used to describe the aerodynamic angles is shown. Lastly, the simplification of the equations of motion to reduce simulation time is discussed.

2.1 Reference frames and kinematics

To describe the dynamics of the constrained flexible wing with FWT the coordinate systems in figure 1 are defined. A body-fixed coordinate system (Index: b) is located at half-chord of the wings root, which is clamped and therefore does not move. The x_b-axis is pointing in root direction from trailing to leading edge. The z_b-axis is pointing downwards and the y_b-axis to the right. For a dihedral of 0° the y_b-axis is located in the wing plane.

To describe the position and motion of the hinge, a hinge-coordinate system (index: h) is used. The hinge coordinate system has its origin in the hinge-axis at half-chord. The x_h-axis is pointing in the direction of the hinge axis from trailing to the leading edge. The y_h axis is defined in the FWT plane, moving with the FWT. The z_h-axis is pointing downwards complementing the right-handed coordinate system.
To describe the orientation of the FWTs profiles and the centre of gravity (CG) of the FWT, a FWT coordinate system (index f) is defined. The FWT coordinate system has its origin in the FWT's CG. For the undeformed wing with zero degrees fold angle, the f-coordinate system has the same orientation as the b-coordinate system.

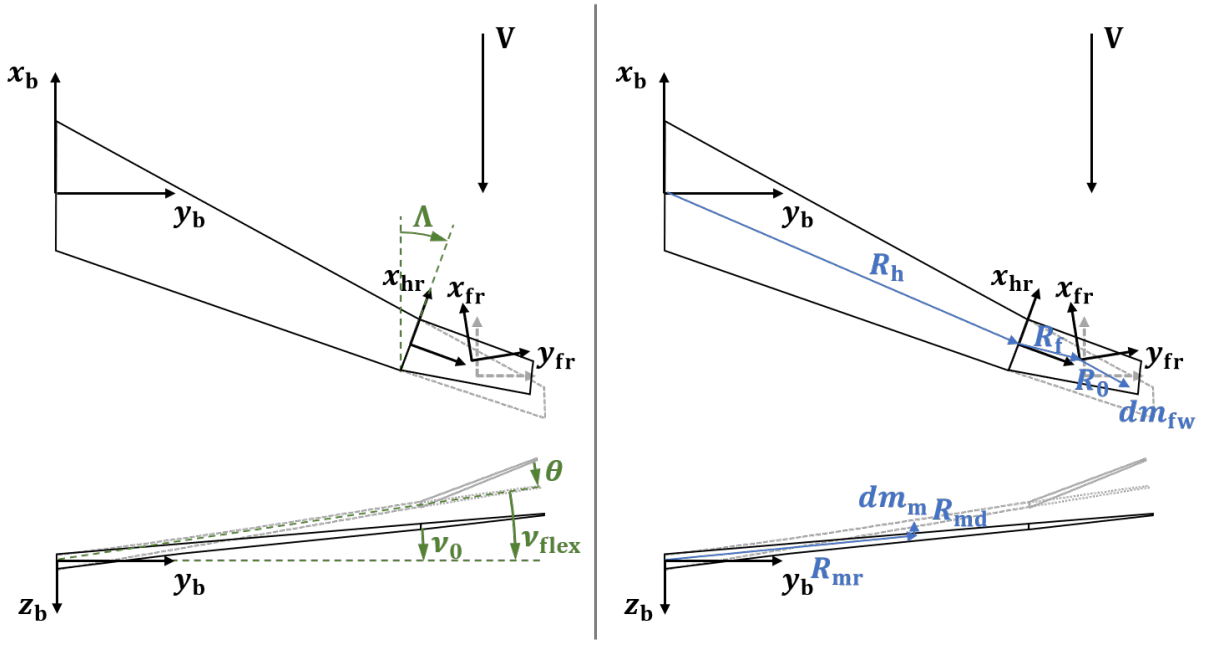

Figure 1: Definition of coordinate systems, angles and position vectors.

As depicted in figure 1, the position of any mass point dm_m of the inner wing can be described by the sum of the position of the point in the undeformed wing $\underline{R}_\mathrm{mr}$ (underscore is used as notation for a vector) and the deformation due to elastic displacement $\underline{R}_\mathrm{md}$:

$$\underline{R}_\mathrm{m} = \underline{R}_\mathrm{mr} + \underline{R}_\mathrm{md}. \tag{3}$$

The elastic displacement is described using modal shapes assuming linear structural dynamics of the wing, apart from the foldable element, which will be treated separately later:

$$\underline{R}_\mathrm{md}|_\mathrm{b} = \underline{\underline{\Phi}}(x_\mathrm{m}, y_\mathrm{m})\big|_\mathrm{b}\, \underline{\eta}(t), \tag{4}$$

wherein $\underline{\underline{\Phi}}(x_\mathrm{m}, y_\mathrm{m})\big|_\mathrm{b}$ is the modal matrix (double underbar is used as notation for a matrix) containing the modal shapes with coordinates written in the body reference frame at position $(x_\mathrm{m}, y_\mathrm{m})$ and $\underline{\eta}(t)$ is the vector of the modal amplitudes. The modal matrix can be obtained by modelling the inner wing in a FEM tool. The velocity of the mass points dm_m expressed and derived in the body axes (indicated in equation 5 by the superscript b) can therefore be described as:

$$\left.\frac{d\underline{R}_\mathrm{m}}{dt}\right|_\mathrm{b}^\mathrm{b} = \underline{\underline{\Phi}}(x_\mathrm{m}, y_\mathrm{m})\big|_\mathrm{b}\, \dot{\underline{\eta}}(t). \tag{5}$$

The position of a mass point dm_{fw} located at the FWT can be described in body axes as the sum of the vector between body and hinge reference frame $\underline{R}_{\mathrm{h}}$, the vector between hinge and FWT reference frame $\underline{R}_{\mathrm{f}}$ and the position vector from the FWT reference frame to the mass point dm_{f} $\underline{R}_0$:

$$\underline{R}_{\mathrm{fw}}|_{\mathrm{b}} = \underline{R}_{\mathrm{h}}|_{\mathrm{b}} + \underline{R}_{\mathrm{f}}|_{\mathrm{b}} + \underline{R}_0|_{\mathrm{b}}\,. \tag{6}$$

Assuming a structural rigid wingtip the vectors can be described by:

$$\underline{R}_{\mathrm{h}}|_{\mathrm{b}} = \underline{R}_{\mathrm{hr}}|_{\mathrm{b}} + \underline{\underline{\Phi}}(x_{\mathrm{h}}, y_{\mathrm{h}})\big|_{\mathrm{b}}\,\underline{\eta}(t), \tag{7}$$

$$\underline{R}_{\mathrm{f}}|_{\mathrm{b}} = \underline{\underline{T}}_{\mathrm{bh}}(t)\;\underline{R}_{\mathrm{f}}|_{\mathrm{h}}\,, \tag{8}$$

$$\underline{R}_0|_{\mathrm{b}} = \underline{\underline{T}}_{\mathrm{bh}}(t)\underline{\underline{T}}_{\mathrm{hf}}\;\underline{R}_0|_{\mathrm{f}}\,, \tag{9}$$

wherein $\underline{R}_{\mathrm{hr}}$ is the position of the hinge coordinate system in the undeformed wing, $\underline{\underline{\Phi}}(x_{\mathrm{h}}, y_{\mathrm{h}})\big|_{\mathrm{b}}$ is the matrix containing the modal shapes in body reference frame at position $(x_{\mathrm{h}}, y_{\mathrm{h}})$. $\underline{\underline{T}}_{\mathrm{bh}}(t)$ is the rotation matrix from the h- to the b-axes orientation and $\underline{\underline{T}}_{\mathrm{hf}}$ the rotation matrix from the f- to h-axes orientation. To rotate from the hinge to the body axes the following rotations (from right to left) are made:

$$\underline{\underline{T}}_{\mathrm{bh}}(t) = \underline{\underline{T}}_{\mathrm{x}}(-\nu_{\mathrm{flex}}(t))\,\underline{\underline{T}}_{\mathrm{y}}(-\varepsilon_{\mathrm{flex}}(t))\,\underline{\underline{T}}_{\mathrm{z}}(-\Lambda)\,\underline{\underline{T}}_{\mathrm{x}}(-\theta(t)), \tag{10}$$

wherein the rotation matrices $\underline{\underline{T}}$ are defined according to Euler angles in the convention 3-2-1 for right-handed coordinate systems. The indices show the associated rotation axis. Thereby, $\theta(t)$ is the fold angle of the FWT, Λ is the hinge line angle, $\varepsilon_{\mathrm{flex}}(t)$ is the incidence angle of the wing (ν_0), including flexibility and $\nu_{\mathrm{flex}}(t)$ is the dihedral angle of the wing (ε_0) including flexibility. To rotate from the FWT to the hinge-axes the following rotation is made:

$$\underline{\underline{T}}_{\mathrm{hf}} = \underline{\underline{T}}_{\mathrm{z}}(\Lambda). \tag{11}$$

The velocity of the mass points dm_{fw} expressed and derived in the body axes can therefore be described as:

$$\begin{aligned}
\left.\frac{d\underline{R}_{\mathrm{fw}}}{dt}\right|_{\mathrm{b}}^{\mathrm{b}} &= \left.\frac{d\underline{R}_{\mathrm{h}}}{dt}\right|_{\mathrm{b}}^{\mathrm{b}} + \left.\frac{d\underline{R}_{\mathrm{f}}}{dt}\right|_{\mathrm{b}}^{\mathrm{b}} + \left.\frac{d\underline{R}_0}{dt}\right|_{\mathrm{b}}^{\mathrm{b}} \\
&= \left.\frac{d\underline{R}_{\mathrm{h}}}{dt}\right|_{\mathrm{b}}^{\mathrm{b}} + \underline{\underline{T}}_{\mathrm{bh}}(t)\left(\left(\left.\frac{d\underline{R}_{\mathrm{f}}}{dt}\right|_{\mathrm{h}}^{\mathrm{h}} + \underline{\omega}_{\mathrm{h}}^{\mathrm{bh}} \times \underline{R}_{\mathrm{f}}|_{\mathrm{h}}\right) + \left(\left.\frac{d\underline{R}_0}{dt}\right|_{\mathrm{h}}^{\mathrm{h}} + \underline{\omega}_{\mathrm{h}}^{\mathrm{bh}} \times \underline{R}_0|_{\mathrm{h}}\right)\right) \\
&= \left.\frac{d\underline{R}_{\mathrm{h}}}{dt}\right|_{\mathrm{b}}^{\mathrm{b}} + \underline{\omega}_{\mathrm{b}}^{\mathrm{bh}} \times \left(\underline{\underline{T}}_{\mathrm{bh}}(t)\,(\underline{R}_{\mathrm{f}}|_{\mathrm{h}} + \underline{R}_0|_{\mathrm{h}})\right),
\end{aligned} \tag{12}$$

wherein

$$\left.\frac{d\underline{R}_{\mathrm{h}}}{dt}\right|_{\mathrm{b}}^{\mathrm{b}} = \underline{\underline{\Phi}}(x_{\mathrm{h}}, y_{\mathrm{h}})\big|_{\mathrm{b}}\,\dot{\underline{\eta}}(t), \tag{13}$$

$$\left.\frac{d\underline{R}_{\mathrm{f}}}{dt}\right|_{\mathrm{h}}^{\mathrm{h}} = \left.\frac{d\underline{R}_0}{dt}\right|_{\mathrm{h}}^{\mathrm{h}} = \underline{0}, \qquad \text{(rigid wingtip)} \tag{14}$$

$$\underline{\omega}_{\mathrm{b}}^{\mathrm{bh}} = \underline{\underline{T}}_{\mathrm{bh}}(t)\;[\dot{\theta}(t), 0, 0]^{\mathrm{T}}\Big|_{\mathrm{h}} + [\gamma_{\mathrm{xh}}, \gamma_{\mathrm{yh}}, 0]^{\mathrm{T}}\,\dot{\underline{\eta}}(t). \tag{15}$$

$\underline{\omega}_{\mathrm{b}}^{\mathrm{bh}}$ is the rotational velocity of the h-axes regarding the b-axes. It can be described as the sum of the angular velocity of the FWT around its hinge $\dot{\theta}$ in b-axes and the angular velocities due

to flexibility of the wing. Assuming small displacements, γ_{xh} and γ_{yh} can be described as the partial y- and x-derivative of the elastic displacement in z in the origin of the hinge coordinate system $(x_{\mathrm{h}}, y_{\mathrm{h}})$:

$$\gamma_{\mathrm{xh}} = \left(\frac{\partial\, \underline{\Phi}_{\mathrm{z}}(x_{\mathrm{h}}, y_{\mathrm{h}})|_{\mathrm{b}}}{\partial y} \right), \tag{16}$$

$$\gamma_{\mathrm{yh}} = -\left(\frac{\partial\, \underline{\Phi}_{\mathrm{z}}(x_{\mathrm{h}}, y_{\mathrm{h}})|_{\mathrm{b}}}{\partial x} \right). \tag{17}$$

2.2 Kinetic energy expression

The kinetic energy of the whole system can be described as the sum of the kinetic energy of the two masses:

$$T = T_{\mathrm{m}} + T_{\mathrm{fw}} = \frac{1}{2} \int_{V_{\mathrm{m}}} \left. \frac{d\underline{R}_{\mathrm{m}}}{dt} \right|_{\mathrm{b}}^{\mathrm{i}} \left. \frac{d\underline{R}_{\mathrm{m}}}{dt} \right|_{\mathrm{b}}^{\mathrm{i}} \rho_{\mathrm{m}} dV_{\mathrm{m}} + \frac{1}{2} \int_{V_{\mathrm{fw}}} \left. \frac{d\underline{R}_{\mathrm{fw}}}{dt} \right|_{\mathrm{b}}^{\mathrm{i}} \left. \frac{d\underline{R}_{\mathrm{fw}}}{dt} \right|_{\mathrm{b}}^{\mathrm{i}} \rho_{\mathrm{fw}} dV_{\mathrm{fw}}. \tag{18}$$

The kinetic energy of the main wing is:

$$T_{\mathrm{m}} = \frac{1}{2} \dot{\underline{\eta}}^{\mathrm{T}}(t) \left(\int_{V_{\mathrm{m}}} \left(\underline{\underline{\Phi}}(x_{\mathrm{m}}, y_{\mathrm{m}})\big|_{\mathrm{b}}^{\mathrm{T}} \underline{\underline{\Phi}}(x_{\mathrm{m}}, y_{\mathrm{m}})\big|_{\mathrm{b}} \right) \rho_{\mathrm{m}} dV_{\mathrm{m}} \right) \dot{\underline{\eta}}(t) = \frac{1}{2} \dot{\underline{\eta}}^{\mathrm{T}}(t) \underline{\underline{\mu}}\, \dot{\underline{\eta}}(t), \tag{19}$$

wherein $\underline{\underline{\mu}}$ is the modal mass matrix of the inner wing which is the identity matrix for mass normalized modal matrices and can be obtained using an FEM tool. The kinetic energy of the FWT can be described as:

$$\begin{aligned}
T_{\mathrm{fw}} = {} & \frac{1}{2} \int_{V_{\mathrm{fw}}} \left(\left. \frac{d\underline{R}_{\mathrm{h}}}{dt} \right|_{\mathrm{b}}^{\mathrm{b}} \left. \frac{d\underline{R}_{\mathrm{h}}}{dt} \right|_{\mathrm{b}}^{\mathrm{b}} \right) \rho_{\mathrm{fw}} dV_{\mathrm{fw}} + \\
& \frac{1}{2} \int_{V_{\mathrm{fw}}} \left(\underline{\omega}_{\mathrm{b}}^{\mathrm{bh}} \times \left(\underline{\underline{T}}_{\mathrm{bh}} \left(\underline{R}_{\mathrm{f}}|_{\mathrm{h}} + \underline{R}_{0}|_{\mathrm{h}} \right) \right) \right) \left(\underline{\omega}_{\mathrm{b}}^{\mathrm{bh}} \times \left(\underline{\underline{T}}_{\mathrm{bh}} \left(\underline{R}_{\mathrm{f}}|_{\mathrm{h}} + \underline{R}_{0}|_{\mathrm{h}} \right) \right) \right) \rho_{\mathrm{fw}} dV_{\mathrm{fw}} + \\
& \int_{V_{\mathrm{fw}}} \left(\left. \frac{d\underline{R}_{\mathrm{h}}}{dt} \right|_{\mathrm{b}}^{\mathrm{b}} \left(\underline{\omega}_{\mathrm{b}}^{\mathrm{bh}} \times \left(\underline{\underline{T}}_{\mathrm{bh}} \left(\underline{R}_{\mathrm{f}}|_{\mathrm{h}} + \underline{R}_{0}|_{\mathrm{h}} \right) \right) \right) \right) \rho_{\mathrm{fw}} dV_{\mathrm{fw}} \\
= {} & \frac{1}{2} m_{\mathrm{fw}} \dot{\underline{\eta}}(t)^{\mathrm{T}} \left. \underline{\underline{\Phi}}(x_{\mathrm{h}}, y_{\mathrm{h}}) \right|_{\mathrm{b}}^{\mathrm{T}} \left. \underline{\underline{\Phi}}(x_{\mathrm{h}}, y_{\mathrm{h}}) \right|_{\mathrm{b}} \dot{\underline{\eta}}(t) + \\
& \frac{1}{2} m_{\mathrm{fw}} \left(\underline{\omega}_{\mathrm{b}}^{\mathrm{bh}} \times \left(\underline{\underline{T}}_{\mathrm{bh}}\, \underline{R}_{\mathrm{f}}|_{\mathrm{h}} \right) \right) \left(\underline{\omega}_{\mathrm{b}}^{\mathrm{bh}} \times \left(\underline{\underline{T}}_{\mathrm{bh}}\, \underline{R}_{\mathrm{f}}|_{\mathrm{h}} \right) \right) + \\
& \frac{1}{2} \left(\underline{\underline{T}}_{\mathrm{fb}} \underline{\omega}_{\mathrm{b}}^{\mathrm{bh}} \right)^{\mathrm{T}} \underline{\underline{J}}_{\mathrm{fw}} \left(\underline{\underline{T}}_{\mathrm{fb}} \underline{\omega}_{\mathrm{b}}^{\mathrm{bh}} \right) + m_{\mathrm{fw}} \left. \underline{\underline{\Phi}}(x_{\mathrm{h}}, y_{\mathrm{h}}) \right|_{\mathrm{b}} \dot{\underline{\eta}}(t) \left(\underline{\omega}_{\mathrm{b}}^{\mathrm{bh}} \times \left(\underline{\underline{T}}_{\mathrm{bh}}\, \underline{R}_{\mathrm{f}}|_{\mathrm{h}} \right) \right).
\end{aligned} \tag{20}$$

Remembering that:

$$\int_{V_{\mathrm{r}}} \underline{R}_{0}|_{\mathrm{f}}\, \rho_{\mathrm{fw}} dV_{\mathrm{fw}} = 0, \tag{21}$$

since the FWT reference frame f is located in the centre of gravity of the rigid wingtip.

2.3 Potential energy expression

The gravitational energy terms of the inner wing U_{gm} and FWT U_{gf} are:

$$U_{\mathrm{gm}} = -\int_{V_{\mathrm{m}}} \underline{R}_{\mathrm{m}}|_{\mathrm{b}} \begin{bmatrix} 0 & 0 & g \end{bmatrix}^{\mathrm{T}} \rho_{\mathrm{m}} dV_{\mathrm{m}} = -\sum_{i=1}^{n_{\mathrm{s}}} m_i (\, z_i|_{\mathrm{b}} + \underline{\Phi}_{\mathrm{z}}(y_i)|_{\mathrm{b}}\, \eta(t)) g, \tag{22}$$

$$U_{\mathrm{gfw}} = -\int_{V_{\mathrm{fw}}} \underline{R}_{\mathrm{fw}}|_{\mathrm{b}} \begin{bmatrix} 0 & 0 & g \end{bmatrix}^{\mathrm{T}} \rho_{\mathrm{fw}} dV_{\mathrm{fw}} = -m_{\mathrm{fw}} \left(\underline{R}_{\mathrm{h}}|_{\mathrm{b}} + \underline{R}_{\mathrm{f}}|_{\mathrm{b}} \right) \begin{bmatrix} 0 & 0 & g \end{bmatrix}^{\mathrm{T}}, \tag{23}$$

wherein m_i is the mass , $z_i|_\mathrm{b}$ the z coordinate and $\underline{\Phi}_\mathrm{z}(y_i)|_\mathrm{b}$ the vector of the z-displacements of the strip i of n_s stripes for every modal shape considered. g is the gravitational constant and m_fw the mass of the FWT. The deformation energy of the inner wing is given by:

$$U_\mathrm{s} = \frac{1}{2}\underline{\eta}^\mathrm{T}(t)\underline{\underline{\gamma}}\,\underline{\eta}(t) = \frac{1}{2}\underline{\eta}^\mathrm{T}\underline{\underline{\mu}}\,\underline{\underline{\omega_\mathrm{n}}}^2\underline{\eta}, \tag{24}$$

wherein $\underline{\underline{\gamma}}$ is the generalised stiffness matrix and $\underline{\underline{\omega_\mathrm{n}}}$ is a diagonal matrix containing the undamped natural frequencies. The spring potential energy can be calculated as follows:

$$U_\mathrm{f} = \frac{1}{2}K_\theta\theta(t)^2, \tag{25}$$

wherein K_θ is the spring stiffness.

2.4 Equations of motion

To derive the equations of motion Lagrange‘s equation is used:

$$\frac{d}{dt}\left(\frac{\partial L}{\partial \dot{q}_k}\right) - \left(\frac{\partial L}{\partial q_k}\right) + \left(\frac{\partial D}{\partial \dot{q}_k}\right) = Q_k \text{ with } L = T - U, D = 0. \tag{26}$$

Thereby q_k are the generalised coordinates and Q_k are the generalised loads. For the constrained wing with FWT the generalised coordinates used are the wingtip fold angle $\theta(t)$ and the modal amplitudes $\underline{\eta}(t)$. The derivation of the generalised loads is described in section 2.5. The resulting equations of motion are complex and will therefore not be printed. The derived equations can be solved analytically in MATLAB/Simulink. As in the future the set of equations shall be derived for the free-flying flexible aircraft, a method to simplify the equations without losing the most important information on the dynamics will be studied in section 2.6.

2.5 Generalized loads and Aerodynamics

The generalised loads are derived for two separate lifting surfaces as follows:

$$Q_k = \int_{V_\mathrm{m}} \underline{f}_\mathrm{m}\frac{\partial \underline{R}_\mathrm{m}|_\mathrm{b}}{\partial q_k}dV_\mathrm{m} + \int_{V_\mathrm{fw}} \underline{f}_\mathrm{fw}\frac{\partial \underline{R}_\mathrm{fw}|_\mathrm{b}}{\partial q_k}dV_\mathrm{fw} + D_\theta\dot{\theta}\frac{\partial \theta}{\partial q_k}, \tag{27}$$

wherein $\underline{f}_\mathrm{m}$ and $\underline{f}_\mathrm{fw}$ are the aerodynamic forces per volume for both volumes and D_θ is the damping value of the hinge rotational damper. For the fold angle that leads to:

$$\begin{aligned} Q_\theta &= \int_{V_\mathrm{fw}} \underline{\underline{T}}_\mathrm{bh}\underline{\underline{T}}_\mathrm{hf}\begin{bmatrix} f_\mathrm{x,fw} & f_\mathrm{y,fw} & f_\mathrm{z,fw}\end{bmatrix}^\mathrm{T}\frac{\partial}{\partial\theta}\left(\underline{\underline{T}}_\mathrm{bh}(\underline{R}_\mathrm{f}|_\mathrm{h} + \underline{R}_0|_\mathrm{h})\right)dV_\mathrm{fw} + D_\theta\dot{\theta} \\ &= y_\mathrm{f}Z_\mathrm{fw} + (M_\mathrm{x} - Y_\mathrm{fw}z_\mathrm{f})\cos(\Lambda) + (M_\mathrm{y} + X_\mathrm{fw}z_\mathrm{f})\sin(\Lambda) + D_\theta\dot{\theta}, \end{aligned} \tag{28}$$

wherein X_fw, Y_fw and Z_fw are the aerodynamic forces in the CG of the FWT in x_f, y_f and z_f direction, respectively M_x and M_y are the moments around the x_f- and y_f-axis. y_f and z_f are the distances of the FWTs CG to the origin of the h-axes. The forces and moments at the FWT are calculated using a quasi-steady approach. So, the aerodynamic loads only depend on the current state. Therefore, the geometric angle of attack at the FWT is calculated in a similar way as in Healy et al. [21] by using rotation matrices to transform the wind vector from the aerodynamic to the FWT reference frame. Therefore, the airspeed is first transformed from the aerodynamic to the body coordinate system by rotating around the sideslip angle β and the angle of attack α:

$$\underline{V}_\mathrm{b} = \underline{\underline{T}}_y(\alpha)\underline{\underline{T}}_z(-\beta)\begin{bmatrix} V & 0 & 0\end{bmatrix}^\mathrm{T}. \tag{29}$$

Then the airspeed is transformed into the h-coordinate system by rotating around the dihedral angle ν_{flex} including the rigid and flexible dihedral, then around the incidence angle $\varepsilon_{\text{flex}}$, also including rigid and flexible incidence, in the sequence around the hinge line angle Λ and finally around the fold angle θ:

$$\underline{V}_{\text{h}} = \underline{\underline{T}}_x(\theta)\underline{\underline{T}}_z(\Lambda)\underline{\underline{T}}_y(\varepsilon_{\text{flex}})\underline{\underline{T}}_x(\nu_{\text{flex}})\underline{V}_{\text{b}}. \tag{30}$$

In the last step the airspeed is transformed back into the f-coordinate system by rotating around the negative hinge line angle $-\Lambda$:

$$\underline{V}_{\text{f}} = \begin{bmatrix} u_{\text{f}} & v_{\text{f}} & w_{\text{f}} \end{bmatrix}^{\text{T}} = \underline{\underline{T}}_z(-\Lambda)\underline{V}_{\text{h}}. \tag{31}$$

The FWT angle of attack α_{fw} and sidelip angle β_{fw} are then calculated as follows (see also appendix A):

$$\alpha_{\text{fw}} = \arctan\left(\frac{w_{\text{f}}}{u_{\text{f}}}\right), \tag{32}$$

$$\beta_{\text{fw}} = \arcsin\left(\frac{v_{\text{f}}}{V}\right). \tag{33}$$

Compared to Healy et al. [21], the wing incidence change due to flexibility is considered and the wing sweep is assumed to be considered within the aerodynamic coefficients.
Reformulating the approach for the angle of attack considering pitch and roll from Silvestre and Paglione [26] to the movement of the FWT we get for each strip s:

$$\alpha_{\text{s}} = \alpha_{\text{fw}} + \dot{\theta}\cos(\Lambda)\frac{x_{\text{AC}}(y_{\text{s}}) - x_{\text{h}}}{u} + \dot{\theta}\sin(\Lambda)\frac{y_{\text{s}} - y_{\text{h}}}{u}. \tag{34}$$

The aerodynamic forces at the FWT can then be calculated as follows [26]:

$$\begin{bmatrix} X_{\text{fw}} \\ Y_{\text{fw}} \\ Z_{\text{fw}} \end{bmatrix} = \int_{b_{\text{h}}}^{b} \underline{\underline{T}}_{\text{fa}} \begin{bmatrix} -d(y) \\ 0 \\ -l(y) \end{bmatrix} dy = \frac{1}{2}\rho V^2 S \underline{\underline{T}}_{\text{fa}} \left(\begin{bmatrix} C_{\text{D0}} \\ 0 \\ C_{\text{L0}} \end{bmatrix} + \begin{bmatrix} C_{\text{D}\alpha} \\ 0 \\ C_{\text{L}\alpha} \end{bmatrix} \alpha + \begin{bmatrix} C_{\text{D}\dot{\theta}} \\ 0 \\ C_{\text{L}\dot{\theta}} \end{bmatrix} \dot{\theta} \right), \tag{35}$$

with

$$\begin{bmatrix} C_{\text{D0}} \\ 0 \\ C_{\text{L0}} \end{bmatrix} = \frac{1}{S}\int_{b_{\text{h}}}^{b} c(y) \begin{bmatrix} C_{\text{d0}}(y) \\ 0 \\ C_{\text{l0}}(y) \end{bmatrix} dy, \tag{36}$$

$$\begin{bmatrix} C_{\text{D}\alpha} \\ 0 \\ C_{\text{L}\alpha} \end{bmatrix} = \frac{1}{S}\int_{b_{\text{h}}}^{b} c(y) \begin{bmatrix} C_{\text{d}\alpha}(y) \\ 0 \\ C_{\text{l}\alpha}(y) \end{bmatrix} dy, \tag{37}$$

$$\begin{bmatrix} C_{\text{D}\dot{\theta}} \\ 0 \\ C_{\text{L}\dot{\theta}} \end{bmatrix} = \frac{1}{S}\int_{b_{\text{h}}}^{b} c(y) \left(\cos(\Lambda)\frac{x_{\text{AC}}(y_{\text{s}}) - x_{\text{h}}}{u} + \sin(\Lambda)\frac{y_{\text{s}} - y_{\text{h}}}{u} \right) \begin{bmatrix} C_{\text{d}\alpha}(y) \\ 0 \\ C_{\text{l}\alpha}(y) \end{bmatrix} dy. \tag{38}$$

The aerodynamic moment at the FWT can be calculated using the same method [26]:

$$\begin{bmatrix} M_x \\ M_y \\ M_z \end{bmatrix} = \underline{r}_{\text{AC}} \times \left(\int_{b_{\text{h}}}^{b} \underline{\underline{T}}_{\text{fa}} \begin{bmatrix} -d(y) \\ 0 \\ -l(y) \end{bmatrix} dy \right) \tag{39}$$

$$= \frac{1}{2}\rho V^2 S D^{**} \left(\begin{bmatrix} C_{\text{Mx0}} \\ C_{\text{My0}} \\ C_{\text{Mz0}} \end{bmatrix} + \begin{bmatrix} C_{\text{Mx}\alpha} \\ C_{\text{My}\alpha} \\ C_{\text{Mz}\alpha} \end{bmatrix} \alpha + \begin{bmatrix} C_{\text{Mx}\dot{\theta}} \\ C_{\text{My}\dot{\theta}} \\ C_{\text{Mz}\dot{\theta}} \end{bmatrix} \dot{\theta} \right), \tag{40}$$

with

$$\begin{bmatrix} C_{\mathrm{Mx0}} \\ C_{\mathrm{My0}} \\ C_{\mathrm{Mz0}} \end{bmatrix} = \frac{D^{**-1}}{S} \int_{b_\mathrm{h}}^{b} \underline{r}_{\mathrm{AC}} \times \left(\underline{\underline{T}}_{\mathrm{fa}} c(y) \begin{bmatrix} C_{\mathrm{d0}}(y) \\ 0 \\ C_{\mathrm{l0}}(y) \end{bmatrix} \right) dy, \tag{41}$$

$$\begin{bmatrix} C_{\mathrm{Mx}\alpha} \\ C_{\mathrm{My}\alpha} \\ C_{\mathrm{Mz}\alpha} \end{bmatrix} = \frac{D^{**-1}}{S} \int_{b_\mathrm{h}}^{b} \underline{r}_{\mathrm{AC}} \times \left(\underline{\underline{T}}_{\mathrm{fa}} c(y) \begin{bmatrix} C_{\mathrm{d}\alpha}(y) \\ 0 \\ C_{\mathrm{l}\alpha}(y) \end{bmatrix} \right) dy, \tag{42}$$

$$\begin{bmatrix} C_{\mathrm{Mx}\dot{\theta}} \\ C_{\mathrm{My}\dot{\theta}} \\ C_{\mathrm{Mz}\dot{\theta}} \end{bmatrix} = \frac{D^{**-1}}{S} \int_{b_\mathrm{h}}^{b} \underline{r}_{\mathrm{AC}} \times \left(\underline{\underline{T}}_{\mathrm{fa}} c(y) \left(\cos(\Lambda) \frac{x_{\mathrm{AC}}(y_\mathrm{s}) - x_\mathrm{h}}{u} + \sin(\Lambda) \frac{y_\mathrm{s} - y_\mathrm{h}}{u} \right) \begin{bmatrix} C_{\mathrm{d}\alpha}(y) \\ 0 \\ C_{\mathrm{l}\alpha}(y) \end{bmatrix} \right) dy. \tag{43}$$

D^{**} is a diagonal matrix containing $[b, c, b]$ in the main diagonal, b is the wingspan, c the mean aerodynamic chord, S the wing area, $\underline{r}_{\mathrm{AC}}$ the aerodynamic centre positions, ρ the air density, V the airspeed. $C_{\mathrm{d0}}(y)$, $C_{\mathrm{l0}}(y)$, $C_{\mathrm{d}\alpha}(y)$ and $C_{\mathrm{l}\alpha}(y)$ are the corresponding aerodynamic coefficients at position y.
The elastic generalised loads for the inner wing are calculated as described in Silvestre [25]. The contribution of the inputs (here: angle of attack α, sideslip angle β and aileron deflection δ_a) to the elastic generalised loads is considered using a quasi-steady approach as in Silvestre and Paglione [26]. The contribution of the elastic deformation on the other hand is considered using an unsteady approach based on Wagner's Function using strip theory [25]. The elastic generalised loads for the FWT are calculated using the following quasi-steady approach:

$$Q_{\eta_\mathrm{i,fw}} = \int_{V_\mathrm{fw}} \underline{\underline{T}}_{\mathrm{bh}} \underline{\underline{T}}_{\mathrm{hf}} \begin{bmatrix} f_{\mathrm{x,fw}} & f_{\mathrm{y,fw}} & f_{\mathrm{z,fw}} \end{bmatrix}^{\mathrm{T}} \frac{\partial}{\partial \eta_i} \left(\underline{\Phi}_i(x_\mathrm{h}, y_\mathrm{h})|_\mathrm{b} \, \eta_i(t) + \underline{\underline{T}}_{\mathrm{bh}}(t) \left(\underline{R}_\mathrm{f}|_\mathrm{h} + \underline{R}_0|_\mathrm{h} \right) \right) dV_\mathrm{fw}, \tag{44}$$

which also leads to a complex equation which will therefore not be printed.

2.6 Simplifying Equations of motion

The derivation of the equations of motion using Lagrange's equation leads to a highly nonlinear complex system of equations, that can be solved numerically using MATLAB/Simulink. As the formulation shall be used for a free-flying flexible aircraft in the future which will involve a more complex system of equations and therefore a longer computational time, there is the need to simplify the equations without losing accuracy. In order to achieve that, the kinetic energy expression is analysed. The only term that significantly simplifies the set of equations of motion without loosing states is the last term in equation 20 (the coupling term between the elastic translatory movement at the hinge and the wingtip rotation). Therefore, the simulation results for the full and the simplified set of equations of motion are analysed in appendix B.
When comparing the simulation results of the full set of equations of motion with the simplified one, it can be seen that when neglecting the coupling term, the average difference during simulation for the analysed variables is less than $5\,\%$, while the maximum difference is less than $10\,\%$ in the analysed case. Simplifying the equation results in an approximately $25\,\%$ faster execution of those equations, which makes the full simulation about $3\,\%$ faster. For the full model a $10\,\mathrm{s}$ simulation takes on average $7.163\,\mathrm{s}$ while the reduced model takes $6.937\,\mathrm{s}$ (using an Intel

Core i7-8700 3.2 GHz processor). The simulation time saved is expected to be higher for more complex systems of equations. So, neglecting the term does not have a large impact on simulation results (see appendix B, page 27, figure 16) and can be a mean of reducing computational time for the simulation.
As the full formulation gives more accurate results and can be solved in a reasonable time frame, the results presented in this paper are calculated using the full formulation.

3 METHODOLOGY

The equations derived in section 2 are used to set up an aeroelastic model in MATLAB/Simulink. The model will then be tested with the TU-Flex aircraft's wing, to which a hinge is added.

3.1 Aeroelastic model

The aeroelastic model is set up in MATLAB/Simulink as shown in figure 2.

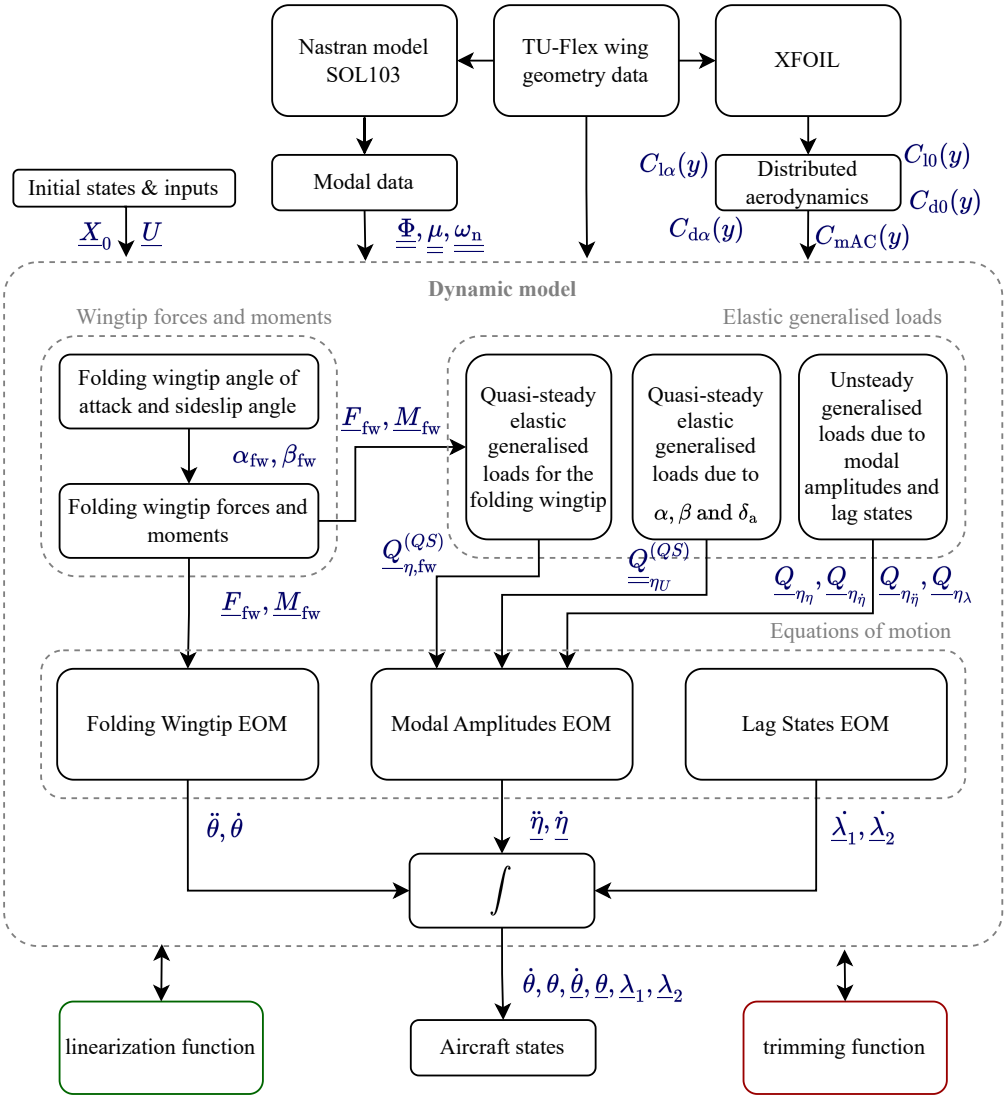

Figure 2: Schematical diagram of aeroelastic model in MATLAB/Simulink.

The input data are the TU-Flex wing geometry, the structural modal base and the distributed linear aerodynamics data. For the modal data the modal matrix $\underline{\underline{\Phi}}$, the modal mass matrix $\underline{\underline{\mu}}$ and the matrix of natural frequencies $\underline{\underline{\omega_{\mathrm{n}}}}$ for the inner flexible wing are needed. These are determined in Nastran by using SOL103. The distributed aerodynamics are determined using XFOIL. As inputs the wind velocity V, the angle of attack α and the sideslip angle β are used.
Within the dynamics block the actual states and inputs are used to first calculate the angle of attack α_{fw} and the sideslip angle β_{fw} of the FWT as shown in subsection 2.5 and appendix B. These are used to calculate the aerodynamic forces $\underline{F}_{\mathrm{fw}}$ and moments $\underline{M}_{\mathrm{fw}}$ in the FWT coordinate system. The forces and moments at the FWT are then used to calculate the quasi-steady elastic generalised loads for the FWT. At the same time the quasi-steady elastic generalised loads due to the inputs and the unsteady elastic generalised loads due to modal amplitudes and lag states are calculated. Then the equations of motion derived in section 2 are used to calculate the state derivatives.
To analyse and compare different trim conditions and the stability of the system a trimming routine and a linearisation function are added.

3.2 Study Case: TU-Flex

As study case the constrained TU-Flex wing with a hinge added to the wing at $80\,\%$ span with a hinge angle of $20°$ is used (table 2). In a first assumption the hinge is assumed to be massless as the results are then compared to the original TU-Flex wing. TU-Flex is a flying demonstrator for flexible aircraft designed to permit easy wing exchange, developed by the Chair of Flight Mechanics, Flight Control, and Aeroelasticity of TU Berlin in cooperation with the DLR's Institute of Aeroelasticity [27].
The distributed aerodynamic data for the new wing with hinge is assumed to be the same as for the original wing, as the geometry of the profiles along the wing do not change. The distributed aerodynamic coefficients for the linear model were derived using XFOIL [28].
The wing model geometry of the original TU-Flex wing was generated using the DLR's internal ModGen/Nastran modelling process [29]. The wing with the FWT was then developed by defining a hinge line at $80\,\%$ span with a hinge line angle of $20°$ along which the elements were split and the outer part of the wing was removed. The modal data of that inner wing is used in the simulation. In table 1 the frequencies of the original TU-Flex wing (TUF) and the cut wing (TUC) using the Nastran models and of the wing with FWT (FWT) using the MATLAB model with a hinge stiffness of $0.2\,\mathrm{Nm/rad}$ and $10\,\mathrm{Nm/rad}$ are shown.

Table 1: Frequencies of the structural modes f in Hz of the original TU-Flex wing (TUF) and the cut wing (TUC) using Nastran and the wing with FWT (FWT) using MATLAB for hinge stiffnesses of $0.2\,\mathrm{Nm/rad}$ and $10\,\mathrm{Nm/rad}$.

		f, Hz			
Mode	Description	TUF	TUC	FWT $K_{\theta,0.2}$	FWT $K_{\theta,10}$
F1	Wingtip rotation	-	-	1.21	5.47
M1	First wing bending	5.25	8.84	6.04	6.04
M2	Second wing bending	20.81	35.62	23.43	23.43
M3	First in-plane wing bending	31.93	53.26	37.16	37.16
M4	Third wing bending	49.68	89.43	53.56	53.56
M5	Forth wing bending	94.03	149.88	101.36	101.35
M6	First wing torsion	120.53	167.66	123.71	123.70
M7	Second in-plane wing bending	125.30	209.42	156.55	156.55
M8	Fifth wing bending	151.64	263.10	221.55	221.55

Table 2: TU-Flex wing with FWT data.

Parameter	Size	Parameter	Size
Minimum speed $V_{\min}$	$18\,\mathrm{m/s}$	Maximum speed $V_{\max}$	$45\,\mathrm{m/s}$
Wing span b	$1.8\,\mathrm{m}$	Wing MAC c	$0.225\,\mathrm{m}$
Wing aspect ratio Λ	16	Leading-edge sweep Λ_0	$20°$
Dihedral Γ	$0°$	Incidence ε	$0°$
Inner wing span	$1.44\,\mathrm{m}$	Folding wingtip span	$0.36\,\mathrm{m}$
Folding wingtip position	$80\,\%$ span	Hinge line angle	$20°$
Inner wing mass m_{iw}	$1.70\,\mathrm{kg}$	Folding wingtip mass m_{fw}	$0.20\,\mathrm{kg}$

4 RESULTS

In this section the trimming and simulation results of the TU-Flex wing with FWT will be compared to the original TU-Flex wing. First the stability of the systems will be analysed looking at the pole-zero-maps and eigenvalue participation. Then the local angles of attack, deflection of the wing in z-direction, as well as total lift and WRBM are compared. Lastly, the results of a simulation of an angle of attack change and an aileron deflection are compared and analysed.

4.1 Stability analysis

To analyse the stability of the system and determine the influence of the states on the modes, the poles and eigenvalues are plotted for different speeds for the TU-Flex wing with FWT (TU-Flex-FWT) and the original TU-Flex wing (TU-Flex). On the left side of figures 3, 4, 5 and 6 the pole positions of the original TU-Flex wing (lighter dashed lines) and the new wing with FWTs (darker solid lines) for speeds between $18\,\mathrm{m/s}$ and $45\,\mathrm{m/s}$ are depicted.
The markers show the position of the poles at the current speed. Poles move from right to left with increasing speed. On the right side of the figures, the impact of different states on the modes at the current speed are visualized for both wings. Values close to one mean a great influence of that state and values close to zero almost no influence of the state. For the case of no rotational hinge damping and a rotational hinge spring stiffness of $0.2\,\mathrm{Nm/rad}$ (figures 3 and 4) it can be seen that a new lower frequency mode (black $\times$) appears. For the $18\,\mathrm{m/s}$ case that new mode is mainly influenced by the θ-states but also influenced by the modal amplitudes η, especially by η_8 which is the structural fifth wing bending. For $45\,\mathrm{m/s}$ both modes are affected by the θ- and the η states. Comparing the modes of both wings, it can be seen that in general the modes of the TU-Flex wing with the FWT element have a higher frequency but are less damped than those of the original TU-Flex wing.
In figures 5 and 6 it can be seen that introducing a rotational hinge damping element of $0.1\,\mathrm{Nms/rad}$ increases the damping of the new lower frequency mode F1* (black $\times$). For a speed of $18\,\mathrm{m/s}$ the influence of the θ-states on that mode is increased.
Overall it can be observed that the interaction between structural modes is higher for the hinged TU-Flex wing.
Figure 7 compares the damping of the M1* and F1* modes with speed for different hinge damping values with that of the M1 mode of the original TU-Flex wing. It can be seen that the damping of the M1 and M1* modes increase with speed while the damping of the F1* mode decreases with speed. Also introducing a FWT reduces considerably the damping of the mode that is mainly affected by the first modal amplitude η_1 (M1), by at least 0.1 which is considered as a drastic drawback of the FWT. Introducing a hinge damping increases the damping of the F1* mode but has almost no effect on the damping of the M1* mode.

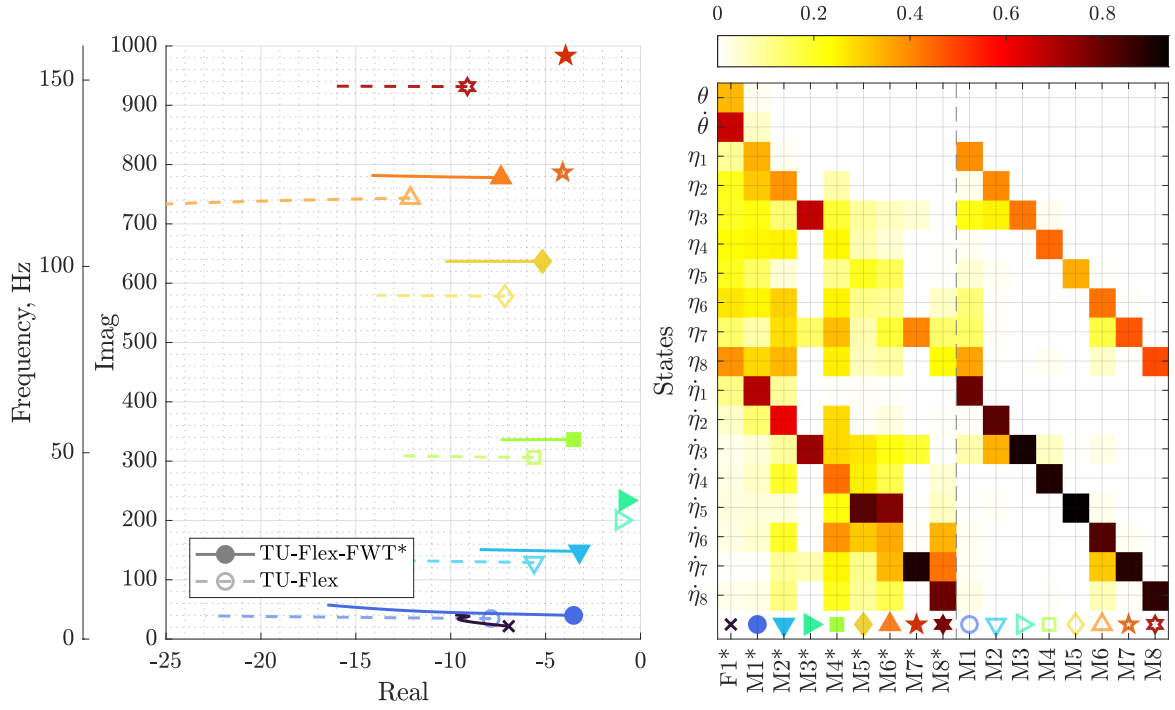

Figure 3: TU-Flex-FWT pole map and eigenvalue participation for $18\,\mathrm{m/s}$ and a rotational spring stiffness of $0.2\,\mathrm{Nm/rad}$ and no rotational damping coefficient.

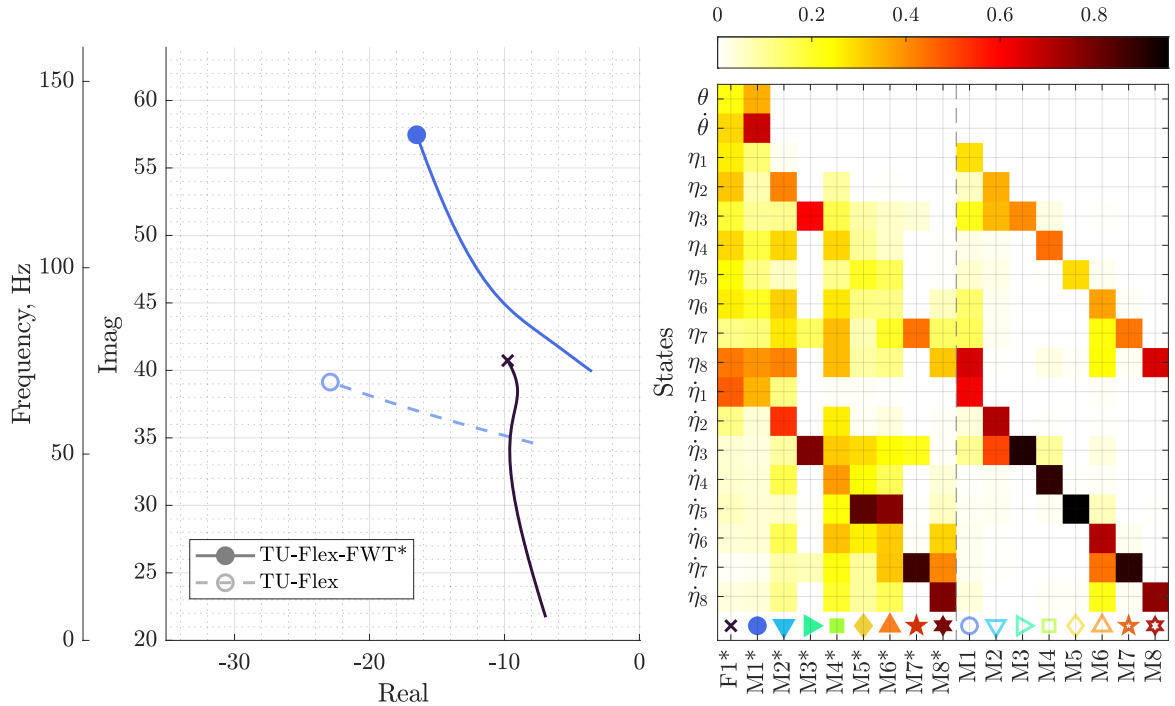

Figure 4: TU-Flex-FWT zoomed pole map and eigenvalue participation for $45\,\mathrm{m/s}$ and a rotational spring stiffness of $0.2\,\mathrm{Nm/rad}$ and no rotational damping coefficient.

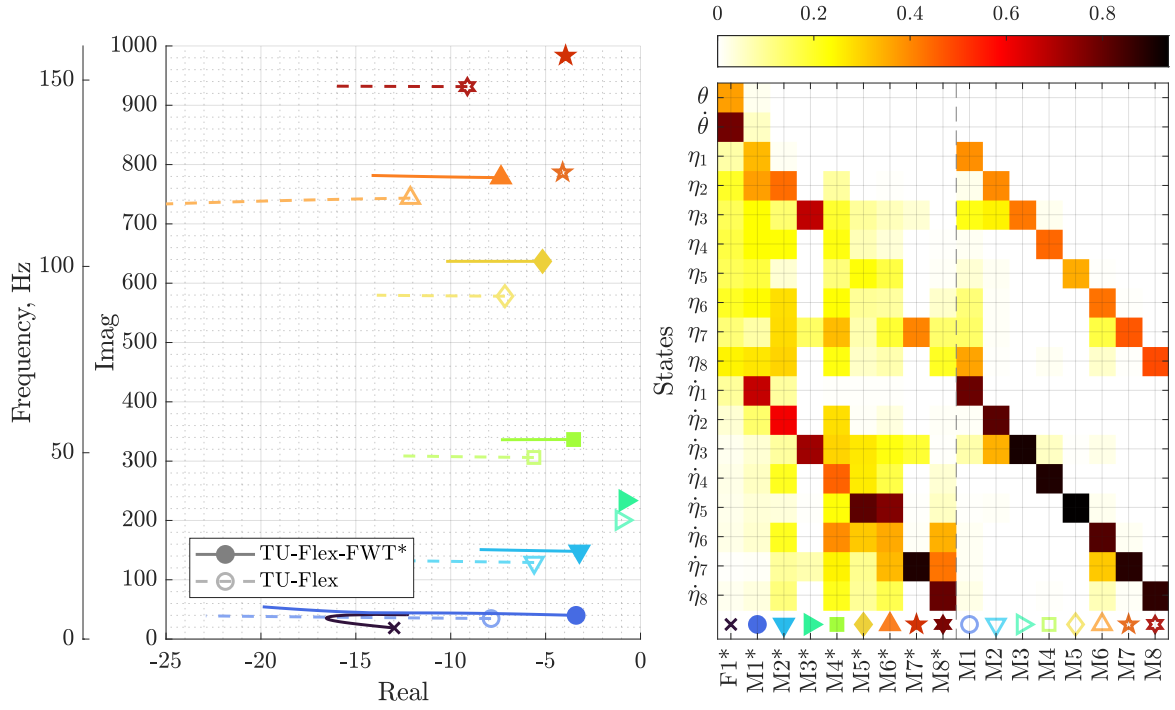

Figure 5: TU-Flex-FWT pole map and eigenvalue participation for $18\,\mathrm{m/s}$ and a spring stiffness of $0.2\,\mathrm{Nm/rad}$ and a rotational damping coefficient of $0.1\,\mathrm{Nms/rad}$.

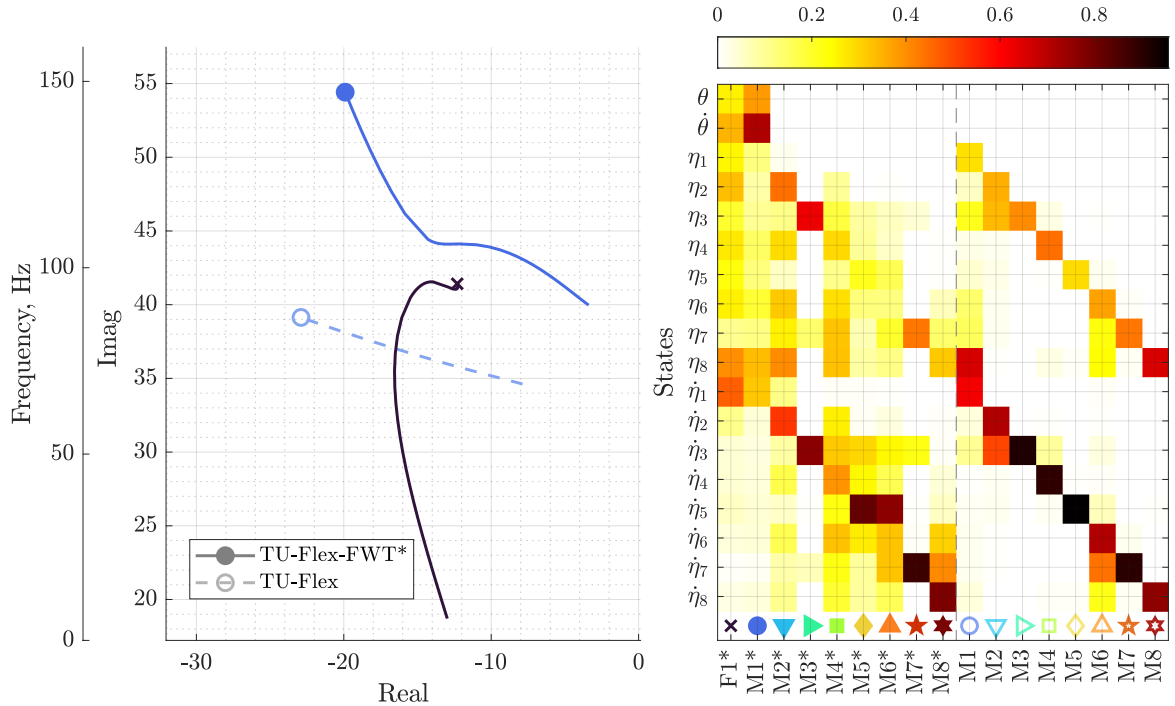

Figure 6: TU-Flex-FWT zoomed pole map and eigenvalue participation for $45\,\mathrm{m/s}$ and a spring stiffness of $0.2\,\mathrm{Nm/rad}$ and a rotational damping coefficient of $0.1\,\mathrm{Nms/rad}$.

As the forces and moments at the FWT are calculated using a quasi-steady approach, the corresponding reduced frequencies for a reference point speed of $30\,\mathrm{m/s}$ shall be analysed. For the first bending that leads to a reduced frequency of $k = 0.040$ and for the FWT mode of $k = 0.019$. As these modes have the main influence in the considered cases a quasi-steady approach is assumed to be sufficient here.

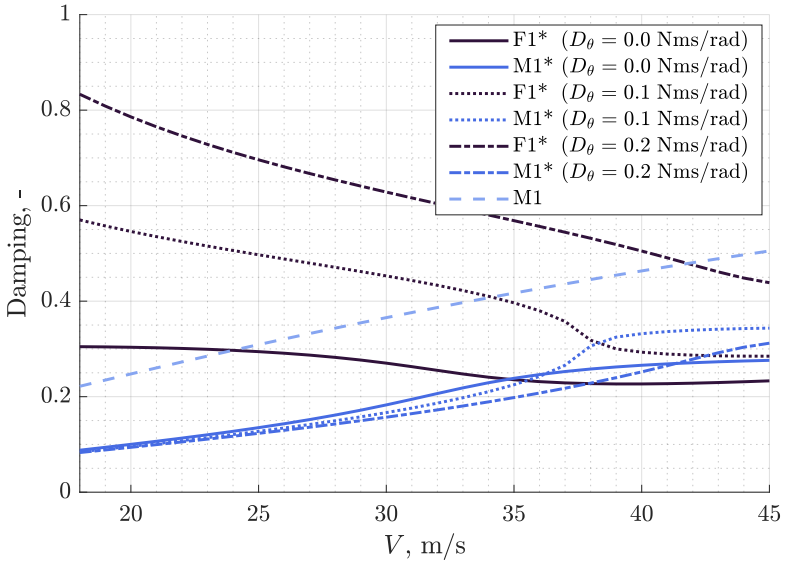

Figure 7: Damping of the original TU-Flex mode M1 and the TU-Flex with folding wingtip modes F1* and M1* for rotational hinge damping values of 0.0, 0.1 and $0.2\,\mathrm{Nms/rad}$ over airspeed V.

4.2 Local angles of attack and local deformation

In figures 8 and 9 the local angle of attack distribution and local deformation and displacement in $-z_\mathrm{b}$ direction for a trim condition are depicted for two different hinge stiffness values of $0.2\,\mathrm{Nm/rad}$ and $10\,\mathrm{Nm/rad}$. It can be seen that for the same angle of attack and airspeed the local angle of attack of the inner wing is higher than for the original TU-Flex wing. That is due to the fact that for zero hinge stiffness, the FWT will always be in a position that creates enough lift to balance its own weight. Therefore, the total lift contributed by the FWT does not change. For the considered condition the total lift and WRBM are lower for the TU-Flex wing with FWT.

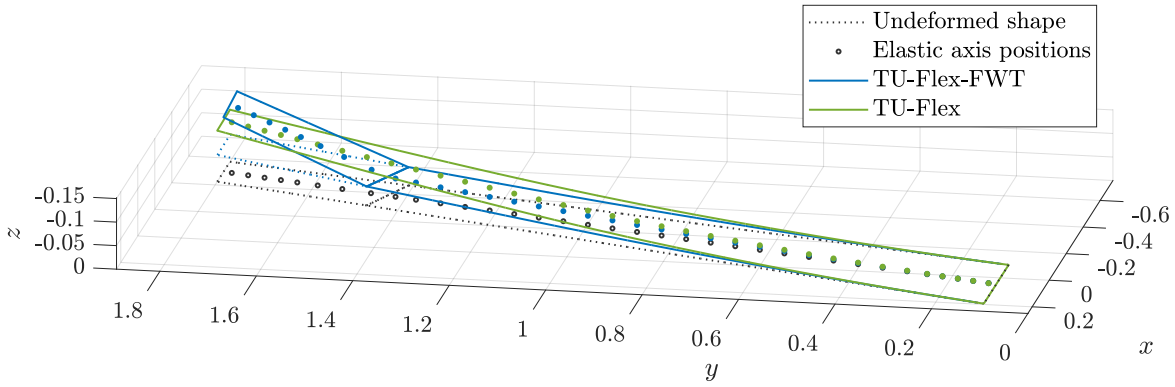

Figure 8: Deformation of the original TU-Flex wing (green) and the TU-Flex wing with FWT (blue) for $30\,\mathrm{m/s}$, an angle of attack of $1°$, a hinge spring stiffness of $0.2\,\mathrm{Nm/rad}$ and no hinge rotational damping coefficient.

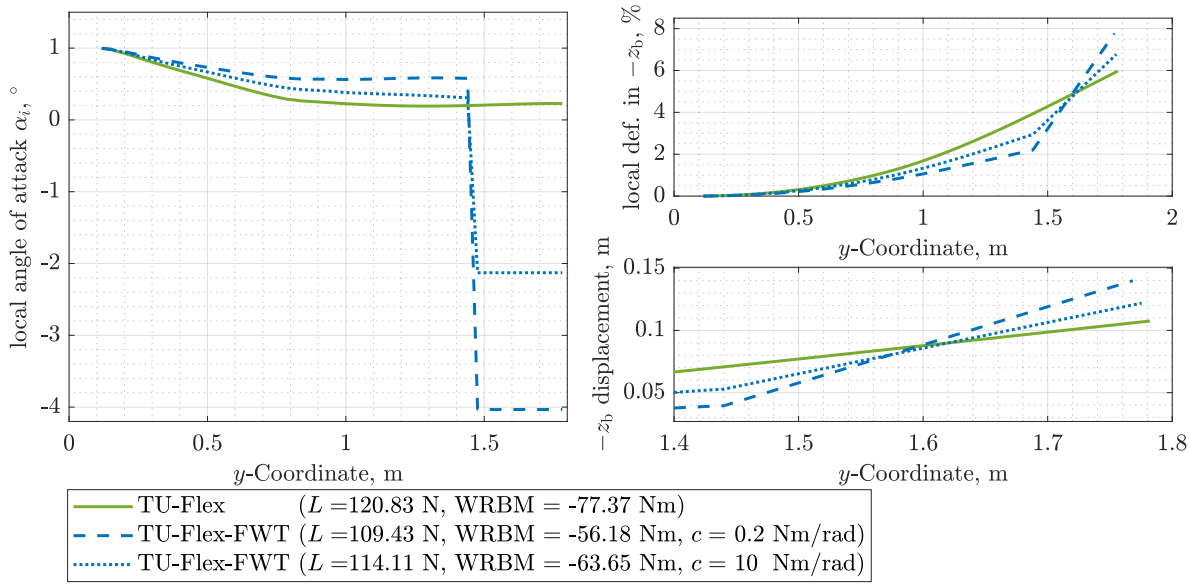

Figure 9: Local angle of attack and local deformation in $-z_b$-direction for the original TU-Flex wing and the TU-Flex wing with FWT for 30 m/s, and angle of attack of 1°, a hinge spring stiffness of 0.2 Nm/rad and 10 Nm/rad and no hinge rotational damping coefficient.

Since in the application for a free-flying aircraft, the wings will need to equilibrate a given weight, it makes sense to trace a comparison for the different wings (with and without FWT) for the same total lift. Therefore, the lift produced by the original wing for a horizontal flight at 30 m/s and $\alpha = 0.87°$ for the free-flying original TU-Flex aircraft is chosen. To create the same total lift the wing with folding wingtip needs to have an angle of attack of $\alpha = 1.47°$ for a hinge spring stiffness of 0.2 m/s and $\alpha = 1.21°$ for a hinge spring stiffness of 10 m/s. In figures 10 and 11 the results for the same total lift are depicted. It can be seen that the angle of attack of the wings with FWTs needed is much higher than that of the original wing. The deformation in z-direction is lower for the wing with FWTs and lower for a low hinge stiffness. The WRBM is smaller for the wings with FWT and the smallest for the low hinge stiffness. So, when both wings produce the same lift the WRBM for the wing with FWT is lower than that of the original TU-Flex wing.

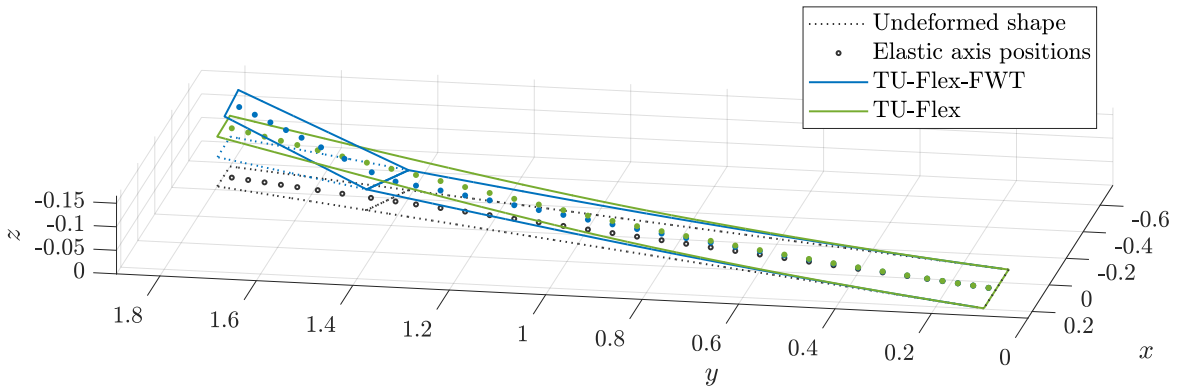

Figure 10: Deformation of the original TU-Flex wing (green) and the TU-Flex wing with FWT (blue) for 30 m/s, and angles of attack of 0.87° and 1.47°, a hinge spring stiffness of 0.2 Nm/rad and no hinge rotational damping coefficient.

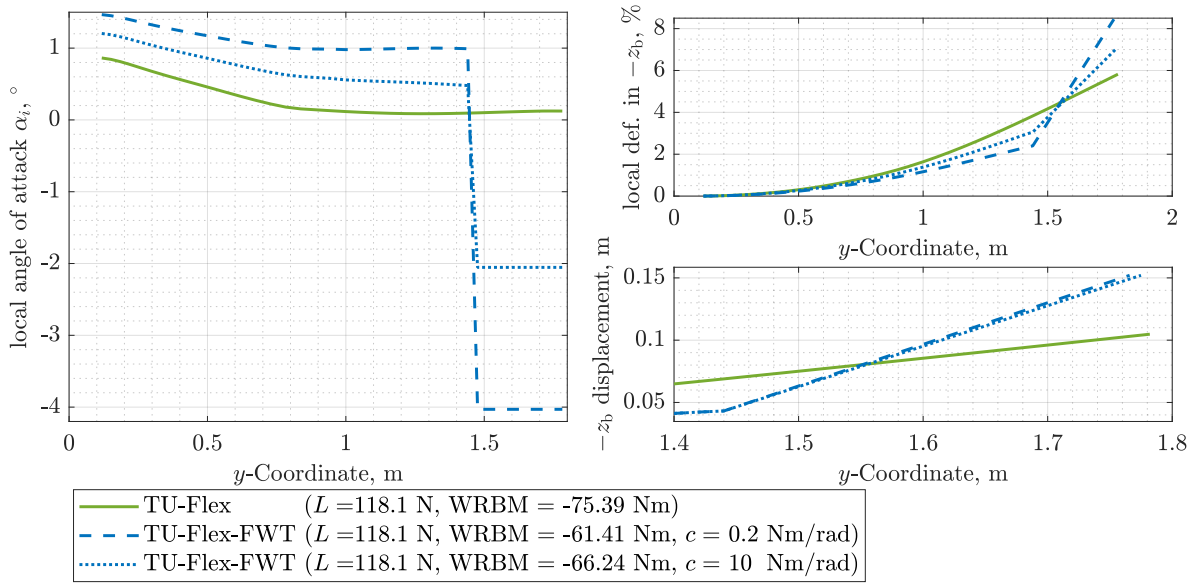

Figure 11: Local angle of attack and local deformation in $-z_b$-direction for the original TU-Flex wing and the TU-Flex wing with FWT for 30 m/s, and angles of attack of 0.87°, 1.47° and 1.21°, a hinge spring stiffness of 0.2 Nm/rad and 10 Nm/rad and no hinge rotational damping coefficient.

4.3 Simulation results: angle of attack and aileron input

In figures 12 and 13 the simulation results for an angle of attack change of 1° after one second of simulation time are shown for the original TU-Flex wing (green dashed) as well as for the wing with FWT with three different rotational hinge damping values of 0.0 (dark blue solid), 0.2 (blue dotted) and 1.0 Nms/rad (light blue dash dot line). For all simulations, the tested wing starts in a position where the same total lift L is generated in the trim condition (30 m/s with $\alpha = 0.87°$ for the original TU-Flex wing and $\alpha = 1.47°$ for the TU-Flex wing with FWT and a hinge stiffness of 0.2 Nm/rad). Displayed in the graphs are the angle of attack at the FWT α_{fw} (upper left), the FWT angle θ (upper right), the deformation in $-z_b$-direction (positive for an upward deflection) at 80 % span in % (middle left), the wing incidence at 80 % span in ° (middle right), the total lift L (lower left) and the absolute value of the WRBM M_r (lower right).
Overall it can be seen that the time response of the original TU-Flex wing is more damped than that of the wing with FWT. The rotational hinge damping coefficient seem to mainly dampen the fold angle θ response while also making the fold angle response slower with increasing hinge damping coefficient. The slower fold angle response leads to higher peaks in deformation in $-z_b$-direction and in wing incidence at 80 % span. So, the higher hinge damping leads to higher peaks in deformation. The deformations are also higher damped for no rotational hinge damping which might be due to the fast and lesser damped reaction of the FWT, which acts against the development of loads, and therefore against moments at the wing root and deformations overall. Nevertheless, the deformation is smaller for the hinged wings than for the original wing.
Regarding the total lift and WRBM the same step of 1° in angle of attack leads to a larger ΔL and ΔWRBM for the original TU-Flex wing, because the change in angle of attack has an influence on the local angles of attack of the whole wing and not mainly the inner wing as for the wing with FWT. The first lift and WRBM peaks do not change with different hinge damping values. The first minimum peak is the largest for a zero hinge damping, which might be due to the lesser damped reaction of the fold angle which also leads to a large reaction in FWT local

angle of attack α_{fw}. After that first minimum the response of the zero damping value is higher damped that that of the higher hinge damping values.
When introducing an abrupt angle of attack change of $1°$ for both wing types it can be seen that the response of the wing with FWT is less damped. The WRBM of the wing with FWT was still smaller than that of the hinged wing, but the higher peaks due to less damping are an important factor that need to be considered and shall be further studied.

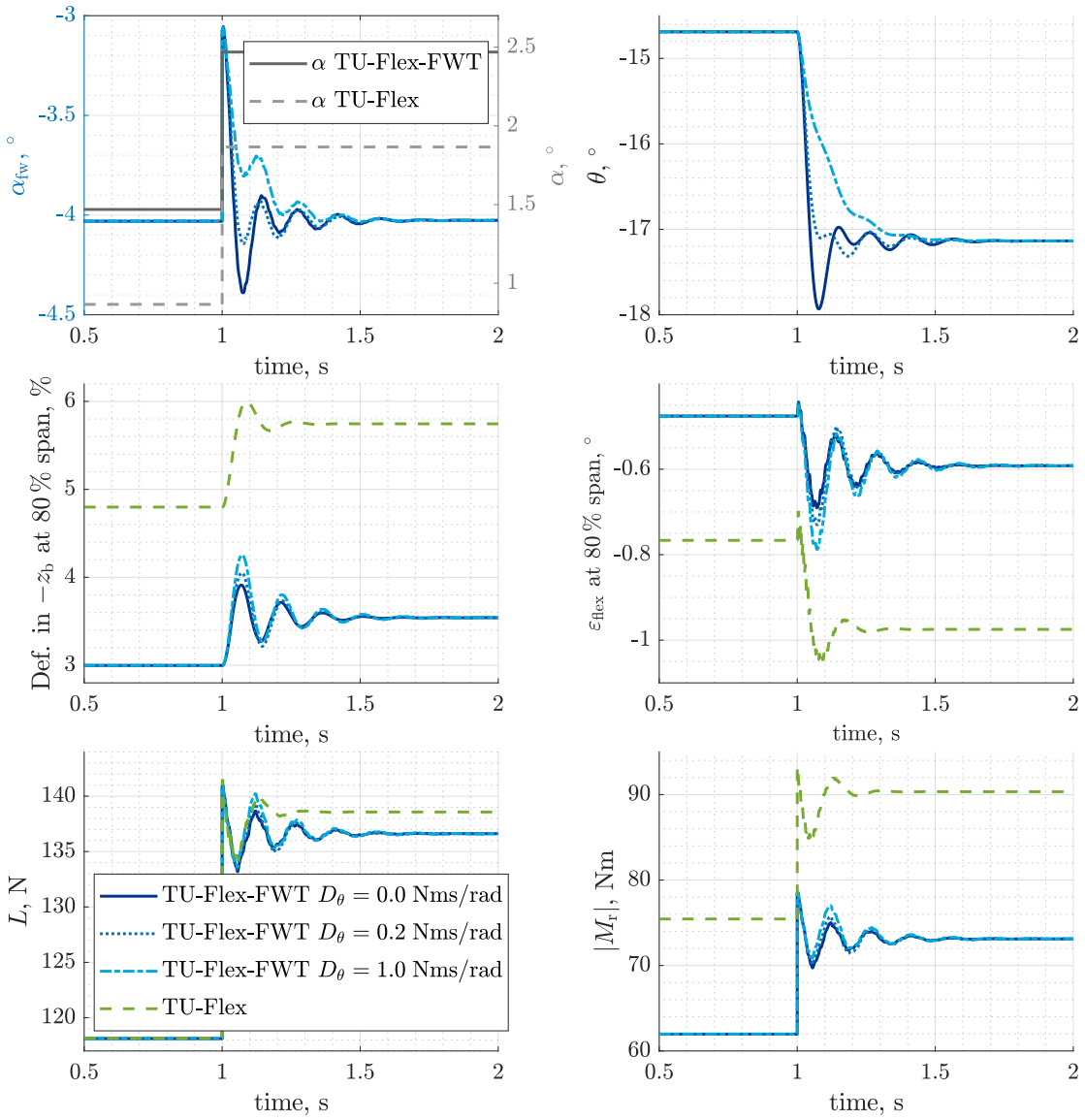

Figure 12: Simulation results for the original TU-Flex wing and the TU-Flex wing with FWT for an angle of attack change of $1°$ after $1\,\text{s}$ for $30\,\text{m/s}$, a spring stiffness of $0.2\,\text{Nm/rad}$ and rotational damping coefficients of 0.0, 0.2 and $1.0\,\text{Nms/rad}$.

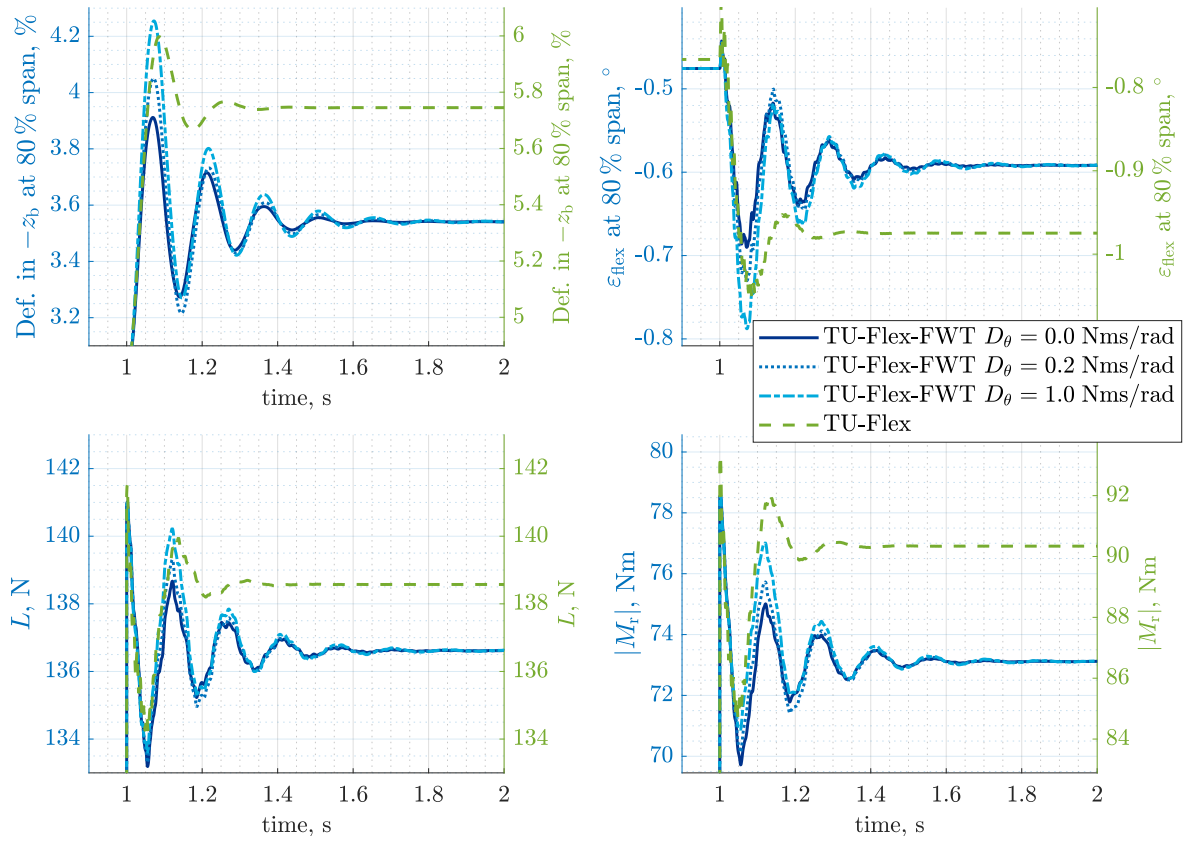

Figure 13: Zoomed simulation results for the original TU-Flex wing and the TU-Flex wing with FWT for an angle of attack change of 1° after 1 s for 30 m/s, a spring stiffness of 0.2 Nm/rad and rotational damping coefficients of 0.0, 0.2 and 1.0 Nms/rad

In figures 14 and 15 the time response to an aileron deflection of 10° is shown. Again, it can be seen that the aileron deflection leads to a change in fold angle θ (upper right) but this time the fold angle becomes smaller in absolute terms. This might be a result of higher deformation of the inner wing at hinge position (80 % span). The aileron deflection leads to a reduction in incidence angle $\varepsilon_{\text{flex}}$ at hinge position, which leads to a decrease in FWT angle of attack α_{fw}, therefore the fold angle θ increases in order to bring the FWT angle of attack back to its original position. It can be seen that the fold angle response is less damped but faster for the wing without hinge damping. This leads to higher initial peaks for the deformation in $-z_b$ and incidence angle $\varepsilon_{\text{flex}}$ at 80 % span. Nevertheless, the response is more damped for the wing without hinge damping due to the faster response of the fold angle. The aileron deflection leads to a higher difference in lift L and WRBM for the wing with hinge then for the original TU-Flex wing. This is due to the higher angle of attack needed for the hinged wing to produce the same lift. For the lift and WRBM again the first peaks are independent of the hinge damping values. After that the first maxima and minima are higher for the wing without hinge damping.
The time response analysis shows that the stability of the system needs to be considered when analysing the load alleviation capabilities of FWTs, as the first response after an angle of attack change or aileron deflection can have a significant impact on the potential of FWT elements to reduce WRBMs. It shows also that different inputs can have different effects on the performance of the FWT.

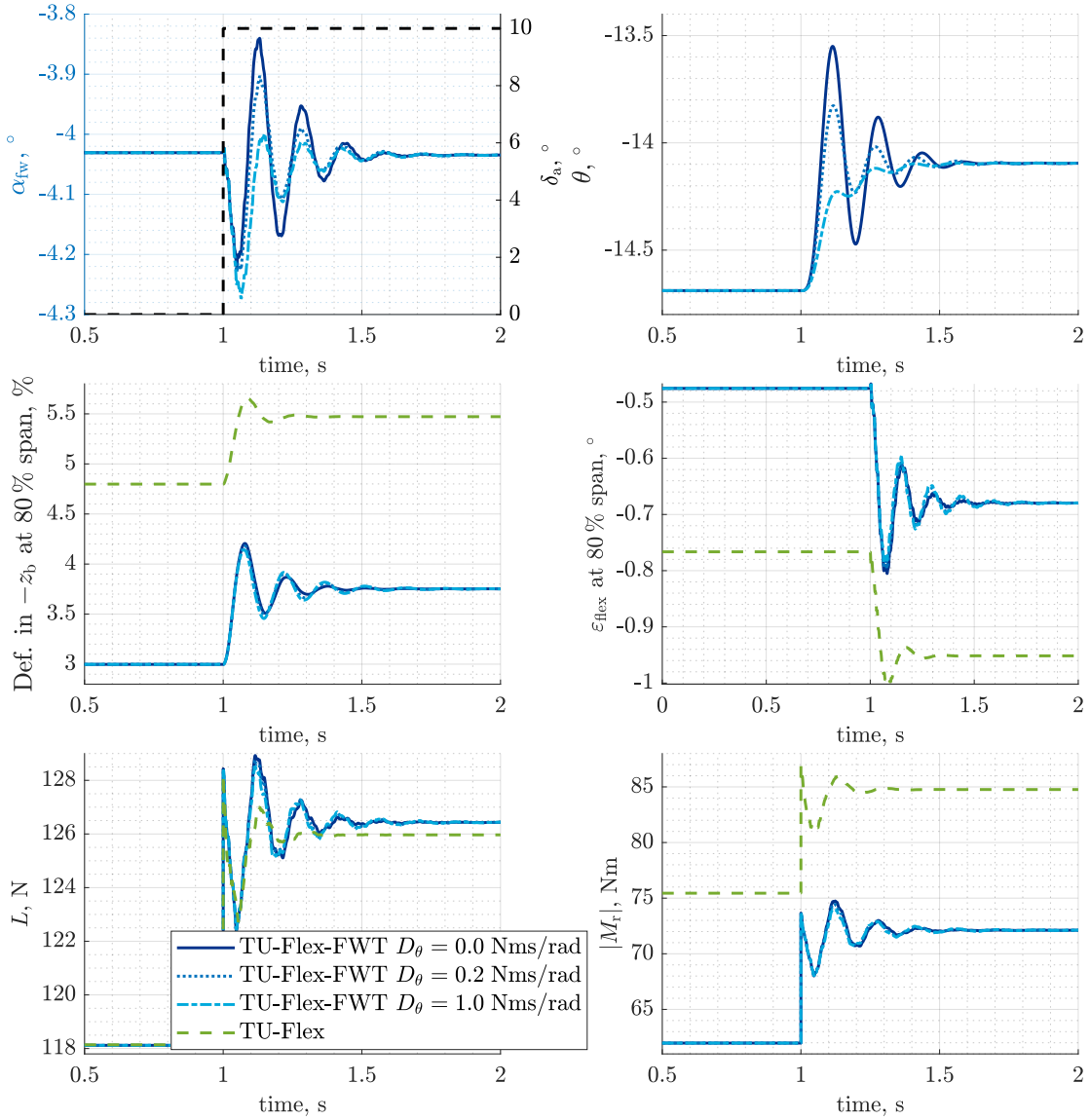

Figure 14: Simulation results for the original TU-Flex wing and the TU-Flex wing with FWT for an aileron deflection of $\delta_{\mathrm{a}} = 10°$ after $1\,\mathrm{s}$ for $30\ \mathrm{m/s}$, a spring stiffness of $0.2\,\mathrm{Nm/rad}$ and rotational damping coefficients of $0.0\,\mathrm{Nms/rad}$ and $0.2\,\mathrm{Nms/rad}$.

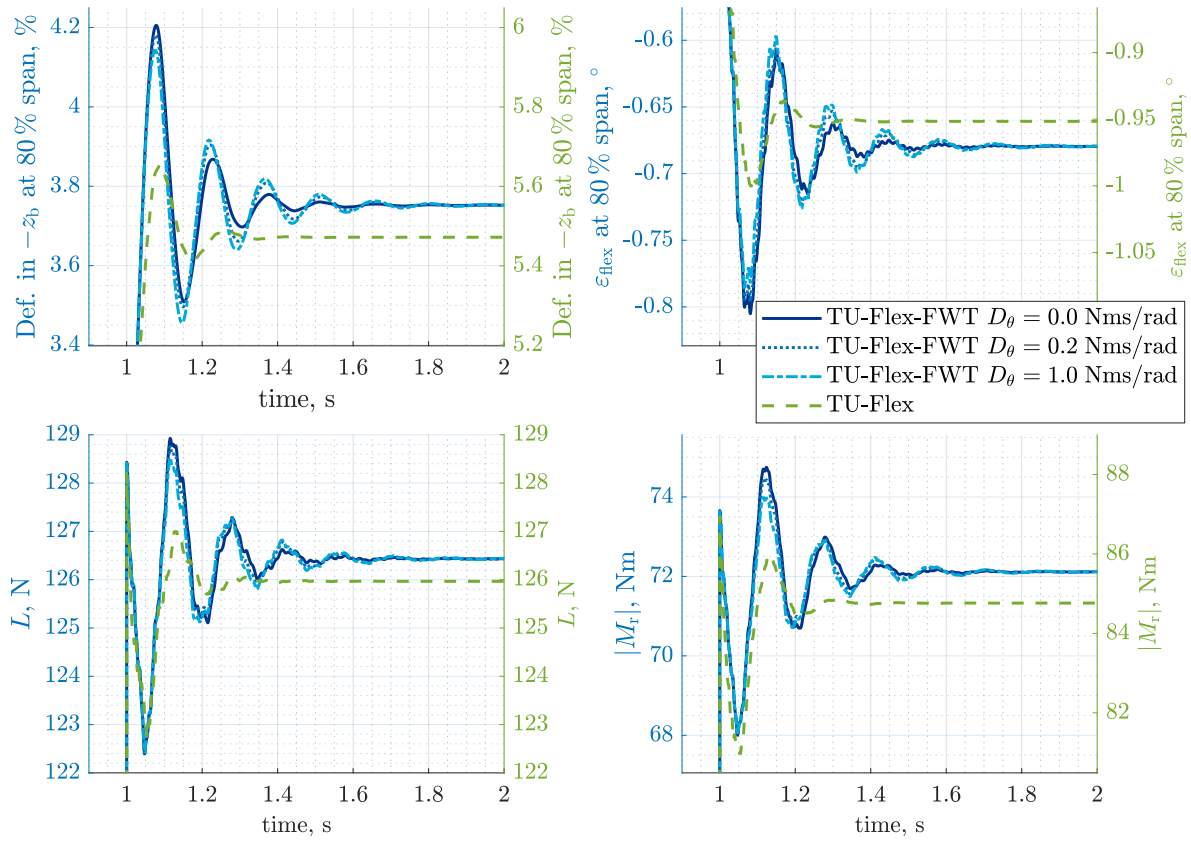

Figure 15: Zoomed simulation results for the original TU-Flex wing and the TU-Flex wing with FWT for an aileron deflection of $\delta_a = 10°$ after 1 s for 30 m/s, a spring stiffness of 0.2 Nm/rad and rotational damping coefficients of 0.0 Nms/rad and 0.2 Nms/rad.

5 SUMMARY

A set of equations of motion describing a constrained flexible wing with flared FWTs is derived applying Lagrange's equation. The model considers follower forces at the inner wing and the FWT and unsteady aerodynamics due to elastic displacements for the inner wing. The follower forces at the FWT are considered by using the geometric exact angle of attack similar to Healy et al. [21]. With the derived equations, an aeroelastic model is set up in MATLAB/Simulink using modal data from Nastran and aerodynamic data from XFOIL.

The trimming and simulation results are tested on the TU-Flex wing with a hinge introduced at 80 % span and then compared to the original TU-Flex wing. For the cases analysed it can be seen that the FWT reduces the stability of the aeroelastic modes. Another lower frequency mode that is mainly influenced by the θ-states close to the frequency of the first bending is introduced to the system and interacts with the first bending. The reduction of stability is an important factor that shall be investigated in the future.

Also, it can be seen that for the investigated cases, the WRBM for producing the same lift is lower than that of the original TU-Flex wing. However, the overall modal damping reduction has as a direct consequence the increase in the WRBM peaks in a dynamic response, thus reducing the FWT potential of a flexible wing in comparison to a rigid one. Also, introducing a hinge damping can make the FWT reaction slower and can lead to higher peaks and a less damped deflection response then without hinge damping. As the considered TU-Flex wing is still very stiff in torsion, it makes sense to analyse less stiff and more flexible wings in the future. For

wings of higher structural flexibility, due to the need of higher angles of attack with FWT, local stall effects will need to be studied in detail.
The model does not yet consider unsteady aerodynamic effects at the FWT due to the complexity that is introduced by considering the geometric nonlinearity in the kinematics of the FWT. That will be considered in a future work. Also, a full free-flying flight dynamic model based on the shown formulation shall be developed in the future, and applied to a transport aircraft considered in the research project GUSTAFO.

6 ACKNOWLEDGEMENTS

This study was financed in part by the German Federal Ministry for Economic Affairs and Climate Action (BMWK) due to a resolution of the German Federal Parliament within the scope of the LuFo VI-2 project GUSTAFO (Grant number 20E2104B).

7 REFERENCES

[1] Rouanet, R. L. M. F. and Rey, F. V. A. J. (1940). Aircraft. U.S. Patent 2,186,558.

[2] Pitt, D. (2004). Static and dynamic aeroelastic analysis of structural wing fold hinges that are employed as an aeroelastic tailoring tool. In 45th AIAA/ASME/ASCE/AHS/ASC Structures, Structural Dynamics & Materials Conference. American Institute of Aeronautics and Astronautics. ISBN 978-1-62410-079-6. doi:10.2514/6.2004-1754.

[3] Pattinson, J., Wilson, T., and Herring, M. (2015). High Fidelity Simulation Of The Folding Wing Tip For Loads Alleviaton. In International Forum on Aeroelasticity and Structural Dynamics IFASD 2015.

[4] Castrichini, A., Hodigere Siddaramaiah, V., Calderon, D., et al. (2015). Nonlinear folding wing-tips for gust loads alleviation. In 56th AIAA/ASCE/AHS/ASC Structures, Structural Dynamics, and Materials Conference. American Institute of Aeronautics and Astronautics. ISBN 978-1-62410-342-1.

[5] Castrichini, A., Hodigere Siddaramaiah, V., Calderon, D., et al. (2016). Preliminary investigation of use of flexible folding wing tips for static and dynamic load alleviation. The Aeronautical Journal, 121, 1–22. ISSN 0001-9240. doi:10.1017/aer.2016.108.

[6] Castrichini, A., Cooper, J. E., Wilson, T., et al. (2017). Nonlinear negative stiffness wingtip spring device for gust loads alleviation. Journal of Aircraft, 54(2), 627–641. doi:10.2514/1.C033887.

[7] Cheung, R. C. M., Rezgui, D., Cooper, J. E., et al. (2018). Testing of a hinged wingtip device for gust loads alleviation. Journal of Aircraft, 55(5), 2050–2067. ISSN 0021-8669, 1533-3868. doi:10.2514/1.C034811.

[8] Cheung, R., Rezgui, D., Cooper, J., et al. (2020). Testing of Folding Wingtip for Gust Load Alleviation of Flexible High-Aspect-Ratio Wing. Journal of Aircraft, 57, 1–13. doi:10.2514/1.C035732.

[9] Wilson, T., Kirk, J., Hobday, J., et al. (2019). Small scale flying demonstration of semi aeroelastic hinged wing tips. In International Forum on Aeroelasticity and Structural Dynamics IFASD 2019.

[10] Wilson, T., Kirk, J., Hobday, J., et al. (2022). Update on AlbatrossONE Semi Aeroelastic Hinge Small Scale Flying Demonstrator Project. In International Forum on Aeroelasticity and Structural Dynamics IFASD 2022.

[11] Castrichini, A., Wilson, T., Saltari, F., et al. (2020). Aeroelastics Flight Dynamics Coupling Effects of the Semi-Aeroelastic Hinge Device. Journal of Aircraft, 57(2), 333–341. doi:10.2514/1.C035602.

[12] Balatti, D., Ellis, J. D., JiffrI, S., et al. (2023). Active hinged wingtip for gust load alleviation and manoeuvres. In AIAA SCITECH 2023 Forum. Reston, Virginia: American Institute of Aeronautics and Astronautics. ISBN 978-1-62410-699-6. doi:10.2514/6.2023-2567.

[13] Balatti, D., Khodaparast, H. H., Friswell, M. I., et al. (2023). Experimental and numerical investigation of an aircraft wing with hinged wingtip for gust load alleviation. Journal of Fluids and Structures, 119, 103892. ISSN 08899746. doi:10.1016/j.jfluidstructs.2023.103892.

[14] Dussart, G., Yusuf, S., and Lone, M. (2019). Identification of In-Flight Wingtip Folding Effects on the Roll Characteristics of a Flexible Aircraft. Aerospace, 6, 63. doi:10.3390/aerospace6060063.

[15] Sanghi, D., Riso, C., Cesnik, C. E. S., et al. (2022). Analaysis of ride qualities in transonic high-aspect-ratio-wing aircraft. In International Forum on Aeroelasticity and Structural Dynamics IFASD 2022.

[16] Sanghi, D., Riso, C., Cesnik, C. E., et al. (2022). Conventional and Unconventional Control Effectors for Load Alleviation in High-Aspect-Ratio-Wing Aircraft. In AIAA SCITECH 2022 Forum. Reston, Virginia: American Institute of Aeronautics and Astronautics. ISBN 978-1-62410-631-6. doi:10.2514/6.2022-4093.

[17] Sanghi, D., Cesnik, C. E., and Riso, C. (2023). Roll Maneuvers of Very Flexible Aircraft with Flared Folding Wingtips. In AIAA SCITECH 2023 Forum. Reston, Virginia: American Institute of Aeronautics and Astronautics. ISBN 978-1-62410-699-6. doi:10.2514/6.2023-0186.

[18] Gatto, A., Bourdin, P., and Friswell, M. I. (2012). Experimental Investigation into the Control and Load Alleviation Capabilities of Articulated Winglets. International Journal of Aerospace Engineering, 2012, 1–15. ISSN 1687-5966, 1687-5974. doi:10.1155/2012/789501.

[19] Ajaj, R. M. (2021). Flight dynamics of transport aircraft equipped with flared-hinge folding wingtips. Journal of Aircraft, 58(1), 98–110. ISSN 1533-3868. doi:10.2514/1.C035940.

[20] Conti, C., Saltari, F., Mastroddi, F., et al. (2021). Quasi-steady aeroelastic analysis of the semi-aeroelastic hinge including geometric nonlinearities. Journal of Aircraft, 58(5), 1168–1178. doi:10.2514/1.C036115.

[21] Healy, F., Cheung, R., Rezgui, D., et al. (2022). On the effect of geometric nonlinearity on the dynamics of flared folding wingtips. Journal of Aircraft, 1–14. doi:10.2514/1.C036877.

[22] Balatti, D., Khodaparast, H. H., Friswell, M. I., et al. (2022). The effect of folding wingtips on the worst-case gust loads of a simplified aircraft model. Proceedings of the Institution of Mechanical Engineers, Part G: Journal of Aerospace Engineering, 236(2), 219–237. doi:10.1177/09544100211010915.

[23] Gu, H., Cheung, R. C., Healy, F., et al. (2023). Experimental Study of the Impact of Folding Wingtip Devices on Aircraft Flight Mechanics and Handling Qualities. In AIAA SCITECH 2023 Forum. Reston, Virginia: American Institute of Aeronautics and Astronautics. ISBN 978-1-62410-699-6. doi:10.2514/6.2023-0402.

[24] Waszak, M. R. and Schmidt, D. K. (1988). Flight dynamics of aeroelastic vehicles. Journal of Aircraft, 25(6), 563571. Place: Legacy CDMS.

[25] Silvestre, F. J. and Luckner, R. (2015). Experimental validation of a flight simulation model for slightly flexible aircraft. AIAA Journal, 53(12), 3620–3636. ISSN 0001-1452. doi:10.2514/1.J054023.

[26] Silvestre, F. J. and Paglione, P. (2008). Dynamics and control of a flexible aircraft. In AIAA Atmospheric Flight Mechanics Conference and Exhibit.

[27] Gonzalez, P., Stavorinus, G., Silvestre, F. J., et al. (2023). TU-flex: A very-flexible flying demonstrator with a generic transport aircraft configuration. In AIAA SCITECH 2023 Forum. American Institute of Aeronautics and Astronautics. ISBN 978-1-62410-699-6. doi:10.2514/6.2023-1312.

[28] García Quesada, A. A., González Ramirez, P. J., Barbosa, G. C., et al. (2024). Influence of nonlinear aerodynamic effects on high aspect ratio aircraft model. In International Forum on Aeroelasticity and Structural Dynamics, (IFASD) 2024.

[29] González, P., Stavorinus, G., Shahi, H., et al. (2022). A preliminary structural design of a flexible flying demonstrator. In ICAS 2022 - 33rd Congress of the International Council of the Aeronautical Sciences, Stockholm , Sweden. ISSN 2958-4647.

COPYRIGHT STATEMENT

APPENDIX A - GEOMETRIC EXACT ANGLE OF ATTACK

In section 2.5 it was described how the geometric angle of attack α_{fw} and sideslip angle β_{fw} at the FWT are described using rotation matrices as in Healy et al. [21]. Other than in Healy et al. [21] it is assumed that the wing sweep is considered within the aerodynamic coefficients but therefore the incidence of the wing is considered in the formulation. That leads to the following

equations for the angle of attack α_{fw} and sideslip angle β_{fw} at the FWT:

$$\begin{aligned}\alpha_{\text{fw}} = &\arctan((-\sin(\beta)(\cos(\Lambda)\cos(\nu_{\text{flex}})\sin(\theta) + (\cos(\varepsilon_{\text{flex}})\cos(\theta) - \\ &\sin(\varepsilon_{\text{flex}})\sin(\theta)\sin(\Lambda))\sin(\nu_{\text{flex}})) + \cos(\beta)(\cos(\alpha)\cos(\theta)\sin(\varepsilon_{\text{flex}}) + \\ &\cos(\varepsilon_{\text{flex}})(\cos(\theta)\cos(\nu_{\text{flex}})\sin(\alpha) + \cos(\alpha)\sin(\theta)\sin(\Lambda)) - \\ &\sin(\alpha)\sin(\theta)(\cos(\nu_{\text{flex}})\sin(\varepsilon_{\text{flex}})\sin(\Lambda) + \cos(\Lambda)\sin(\nu_{\text{flex}}))))/ \\ &(\cos(\alpha)\cos(\beta)(-\sin(\varepsilon_{\text{flex}})\sin(\theta)\sin(\Lambda) + \cos(\varepsilon_{\text{flex}})(\cos(\Lambda)^2 + \cos(\theta)\sin(\Lambda)^2)) + \\ &\sin(\beta)(\cos(\nu_{\text{flex}})\sin(\theta/2)^2\sin(2\Lambda) + (\cos(\varepsilon_{\text{flex}})\sin(\theta)\sin(\Lambda) + \sin(\varepsilon_{\text{flex}})(\cos(\Lambda)^2 + \\ &\cos(\theta)\sin(\Lambda)^2))\sin(\nu_{\text{flex}})) + \cos(\beta)\sin(\alpha)(-\cos(\nu_{\text{flex}})(\cos(\varepsilon_{\text{flex}})\sin(\theta)\sin(\Lambda) + \\ &\sin(\varepsilon_{\text{flex}})(\cos(\Lambda)^2 + \cos(\theta)\sin(\Lambda)^2)) + \sin(\theta/2)^2\sin(2\Lambda)\sin(\nu_{\text{flex}})))), \end{aligned} \tag{45}$$

$$\begin{aligned}\beta_{\text{fw}} = &\arcsin(\sin(\Lambda)(\cos(\alpha)\cos(\beta)\cos(\varepsilon_{\text{flex}})\cos(\Lambda) + \sin(\beta)(\cos(\nu_{\text{flex}})\sin(\Lambda) + \\ &\cos(\Lambda)\sin(\varepsilon_{\text{flex}})\sin(\nu_{\text{flex}})) + \cos(\beta)\sin(\alpha)(-\cos(\Lambda)\cos(\nu_{\text{flex}})\sin(\varepsilon_{\text{flex}}) + \\ &\sin(\Lambda)\sin(\nu_{\text{flex}}))) + \cos(\Lambda)(\cos(\alpha)\cos(\beta)(\sin(\varepsilon_{\text{flex}})\sin(\theta) - \\ &\cos(\varepsilon_{\text{flex}})\cos(\theta)\sin(\Lambda)) + \sin(\beta)(\cos(\theta)\cos(\Lambda)\cos(\nu_{\text{flex}}) - \\ &(\cos(\varepsilon_{\text{flex}})\sin(\theta) + \cos(\theta)\sin(\varepsilon_{\text{flex}})\sin(\Lambda))\sin(\nu_{\text{flex}})) + \\ &\cos(\beta)\sin(\alpha)(\cos(\varepsilon_{\text{flex}})\cos(\nu_{\text{flex}})\sin(\theta) + \cos(\theta)(\cos(\nu_{\text{flex}})\sin(\varepsilon_{\text{flex}})\sin(\Lambda) + \\ &\cos(\Lambda)\sin(\nu_{\text{flex}})))), \end{aligned} \tag{46}$$

wherein α is the global angle of attack, β is the global sideslip angle, Λ is the hinge line angle, $\varepsilon_{\text{flex}}$ is the incidence angle at hinge coordinate system position, which is a sum of geometric incidence and incidence due to flexibility of the wing and ν_{flex} is the dihedral at hinge coordinate system position, which is a sum of geometric dihedral and dihedral due to flexibility of the wing.

APPENDIX B - SIMPLIFYING EQUATIONS OF MOTION

In section 2.6 a way to simplify the set of equations of motion was described. In this section the difference between the full and the simplified model shall be analysed. Therefore, the simulation results for an angle of attack change of 1° are compared (figure 16), starting from the trim condition of $30\,\mathrm{m/s}$ and angle of attack of 1.47°, which is also used in section 4.3. It can be seen that the simplified simulation has a small amplitude and phase difference. The average and maximum difference in fold angle θ, deformation in $-z_{\text{b}}$ direction at $80\,\%$ span and incidence angle $\varepsilon_{\text{flex}}$ at $80\,\%$ span for the simulation between $1\,\text{s}$ and $1.5\,\text{s}$ simulation time are shown in table 3. It can be seen that the average difference is less than $5\,\%$, while the maximum difference is smaller than $10\,\%$ for the analysed case.

Table 3: Average and maximum difference in fold angle θ, deformation in $-z_{\text{b}}$ direction at $80\,\%$ span and incidence angle $\varepsilon_{\text{flex}}$ at $80\,\%$ span for the simulation between $1\,\text{s}$ and $1.5\,\text{s}$.

Variable	Average difference, %	Maximum difference, %
Fold angle θ	0.31	0.95
Deformation in $-z_{\text{b}}$ at $80\,\%$ span	1.60	5.27
Incidence angle $\varepsilon_{\text{flex}}$ at $80\,\%$ span	2.59	8.51

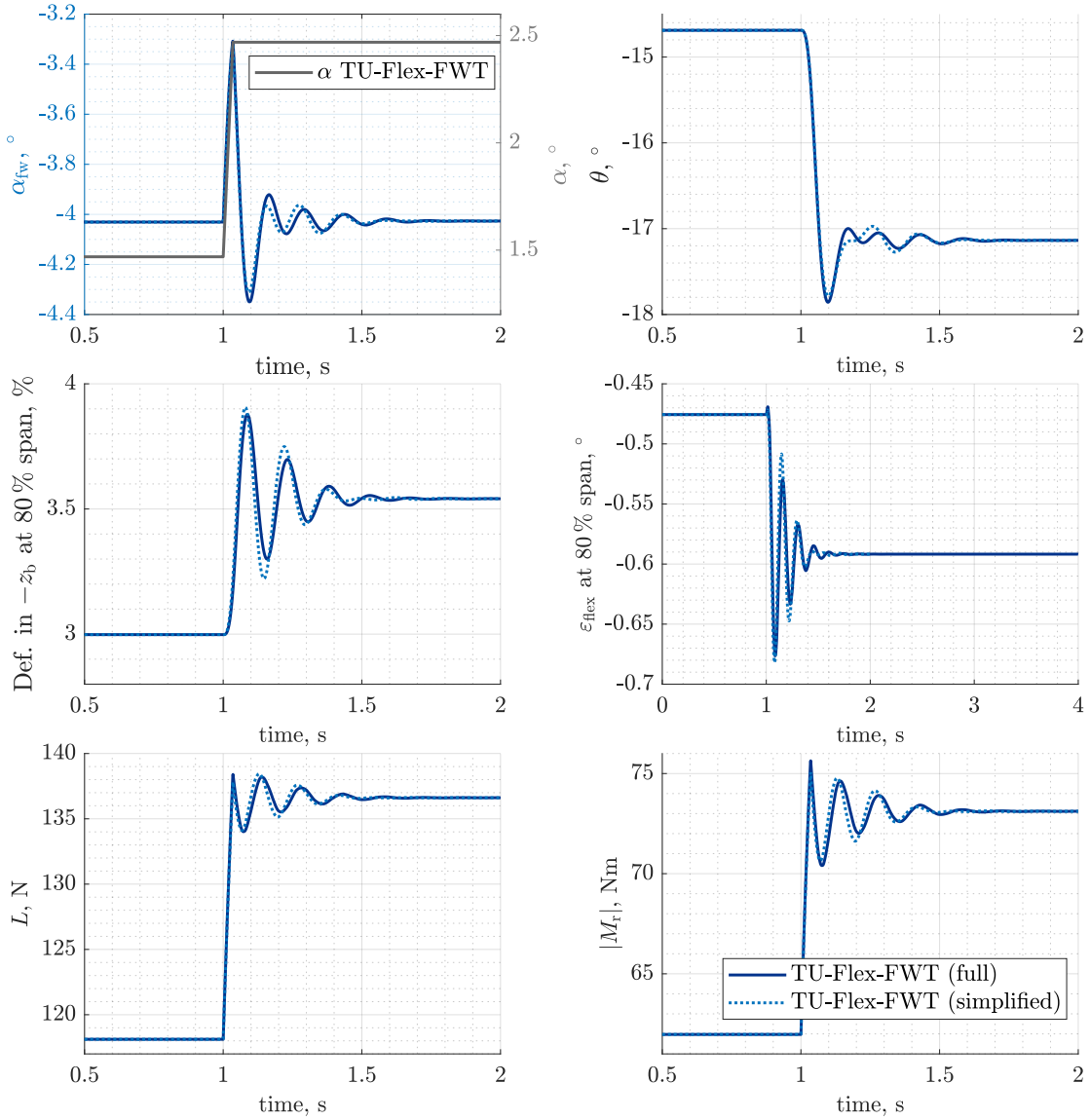

Figure 16: Simulation results for the full and simplified equations for the TU-Flex wing with FWT for an angle of attack change of 1° after $1\,\mathrm{s}$ for $30\ \mathrm{m/s}$, a spring stiffness of $0.2\,\mathrm{Nm/rad}$ and rotational damping coefficients of $0.0\,\mathrm{Nms/rad}$.